REVIEW

Check for updates

Recent advances in 2D/nanostructured metal sulfide-based gas sensors: mechanisms, applications, and perspectives

Hongyu Tang, [ID] [a] Leandro Nicolas Sacco,[a] Sten Vollebregt,[a] Huaiyu Ye, [ID] [bc] Xuejun Fan*[d] and Guoqi Zhang*[a]

2D and nanostructured metal sulfide materials are promising in the advancement of several gas sensing applications due to the abundant choice of materials with easily tunable electronic, optical, physical, and chemical properties. These applications are particularly attractive for gas sensing in environmental monitoring and breath analysis. This review gives a systematic description of various gas sensors based on 2D and nanostructured metal sulfide materials. Firstly, the crystal structures of metal sulfides are introduced. Secondly, the gas sensing mechanisms of different metal sulfides based on density functional theory analysis are summarised. Various gas-sensing concepts of metal sulfide-based devices, including chemiresistors, functionalized metal sulfides, Schottky junctions, heterojunctions, field-effect transistors, and optical and surface acoustic wave sensors, are compared and presented. It then discusses the extensive applications of metal sulfide-based sensors for different gas molecules, including volatile organic compounds (*i.e.*, acetone, benzene, methane, formaldehyde, ethanol, and liquefied petroleum gas) and inorganic gas (*i.e.*, CO_2, O_2, NH_3, H_2S, SO_2, NO_x, CH_4, H_2, and humidity). Finally, a strengths−weaknesses−opportunities−threats (SWOT) analysis is proposed for future development and commercialization in this field.

1. Introduction

Nanostructured materials have been considered promising candidates for gas sensing applications due to their large surface area, abundant surface-active sites, and high surface reactivity.[1] They are primarily used for monitoring air quality, the environmental situation, and breath. Typically, atmospheric pollutants include nitrogen dioxide (NO_2), nitrogen monoxide (NO), ammonia (NH_3), hydrogen sulfide (H_2S), sulfur dioxide (SO_2), carbon monoxide (CO), carbon dioxide (CO_2), methane (CH_4), and volatile organic compounds (VOCs).[2] When these pollutants exceed the recommended exposure limits, they have negative effects on the environment and human health (Table 1). Therefore, the gas sensor needs to detect different gases simultaneously with high sensitivity and selectivity, a small size, low cost, and low power consumption (<10 mW).[3] In the aspect of breath analysis, different biomarkers from exhaled breath

need to be recognized accurately.[4] Normally, human breath contains nitrogen (N_2), oxygen (O_2), CO_2, hydrogen (H_2), inert gases, and water vapour. Sometimes, it includes organic VOCs *viz.* acetone, ethanol, isoprene, ethane, methane, pentane, *etc.*, and inorganic gases such as NO_x, NH_3, CO_x, and H_2S, see Fig. 1a. These excretory products diffuse into the inhaled air in the alveoli of the lungs and are then ejected in the form of exhaled air. Therefore, exhaled air carries different biomarkers, which can be used as fingerprints of metabolic products. This enables early diagnosis and prevention of respiratory diseases such as lung cancer, diseases of the kidneys, prostate, and bladder, and even Parkinson's disease, see Fig. 1b.[5,6] However, the maximum permissible limits of biomarkers are mostly at the parts-per-billion (ppb) level, which requires a highly sensitive gas sensor with a low limit of detection (LOD).

Solid-state sensors such as metal oxide semiconductors (MOSs),[9] carbon-based nanomaterials (CNMs),[10–12] and metal sulfide semiconductors[13] are used extensively in gas detection research. After Taguchi patented the first oxide-based gas sensor in 1962, various high sensitivity and low-cost gas sensors based on MOSs have been developed.[14] Tungsten oxide (WO_3) nanotubes have been proved as a potential MOS for the detection of NO at the ppb level.[15] Orthorhombic molybdenum trioxide (α-MoO_3) nanoribbons can detect NH_3 down to 280 ppt.[16] Gas sensors based on Pt functionalized tin dioxide (SnO_2)[17] or indium oxide (In_2O_3)[18] can detect the lowest acetone

[a]Department of Microelectronics, Faculty of Electrical Engineering, Mathematics & Computer Science, Delft University of Technology, Delft 2628 CT, The Netherlands. E-mail: G.Q.Zhang@tudelft.nl

[b]School of Microelectronics, Southern University of Science and Technology, Shenzhen 518055, China

[c]Shenzhen Institute of Wide-Bandgap Semiconductors, Shenzhen 518055, Guangdong, China

[d]Department of Mechanical Engineering, Lamar University, Texas 77710, USA. E-mail: xfan@lamar.edu

This journal is © The Royal Society of Chemistry 2020

J. Mater. Chem. A, 2020, **8**, 24943–24976 | **24943**

Table 1 The environmental and human health impacts of different air pollutants and their maximum permissible limits set by the European Union[7,8]

Gas	Environmental and human health impact	Maximum permissible limit		Value of interest (ppb)
		8 hours (ppm)	Short-term (15 min, ppm)	
NO_2	Indirect green house gas, acidification, eutrophication, cardiovascular mortality, asthma, lung function	0.5	1	21
NH_3	Toxic, $PM_{2.5}$ precursor	20	50	20 000
H_2S	SO_2 precursor, toxic	5	10	5000
SO_2	Indirect green house gas, acidification, particulate matter, precursor, cardiovascular mortality	0.5	1	7.5
CO	Indirect green house gas, toxic, asthma, cardiovascular disease, cardiac disease, psychiatric admissions, etc.	20	100	4000
CO_2	Green house gas – climate change	5000	—	400 000
CH_4	Green house gas – climate change	1000	—	1800

concentration of 10 ppb. The $ZnSnO_3$ gas sensor can detect 100 ppb ethanol.[19] Many MOS-based devices can detect H_2S at less than 1 ppm, such as copper oxide (CuO), SnO_2, In_2O_3, zinc oxide (ZnO), titanium oxide (TiO_2), and iron oxide (Fe_2O_3).[20] However, the operating temperature (OT) of MOS-based devices is usually high (100–300 °C), which induces high power consumption and consequently hinders the gas-sensing applications. CNMs, such as graphene and its derivatives and carbon nanotubes (CNTs), were employed as chemical gas sensors owing to their outstanding characteristics of a mesoporous nature, a large specific surface area, and enhanced electron transport properties.[21] Pristine reduced graphene oxide (rGO) can detect NH_3 and NO_x, and rGO with a functionally modified surface (such as rGO/ZnO, rGO/Pt, and rGO/Ni) are known to detect VOCs (such as acetone, phenol, and nitrobenzene).[22–24] Rigoni et al.[25] recently demonstrated an NH_3 sensor comprising pristine SWCNTs that had a LOD of 3 ppb. The review of

graphene-based[26] and CNT-based[12] chemical sensors reported that 2D/nano-materials have great potential applications in gas detection and proposed several techniques to improve gas-sensing performance, which can be extended to other materials, for instance, metal sulfides.

Lots of metal sulfide-based sensors can work at room temperature and have lower power consumption, making them superior to MOS-based sensors.[27] The sensing performances of metal sulfides are similar to those of CNM-based devices, except for their sizeable and tunable bandgaps, making such materials suitable for transistor applications, further inducing unique
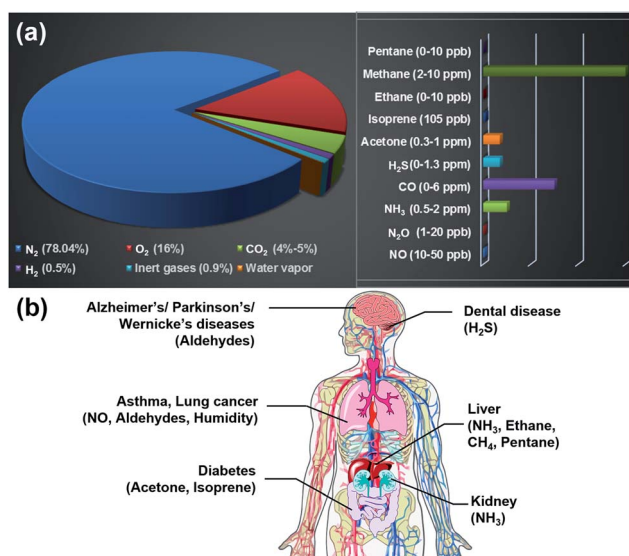
Fig. 1 (a) The gas contents of human breath and (b) the biomarkers of different diseases.
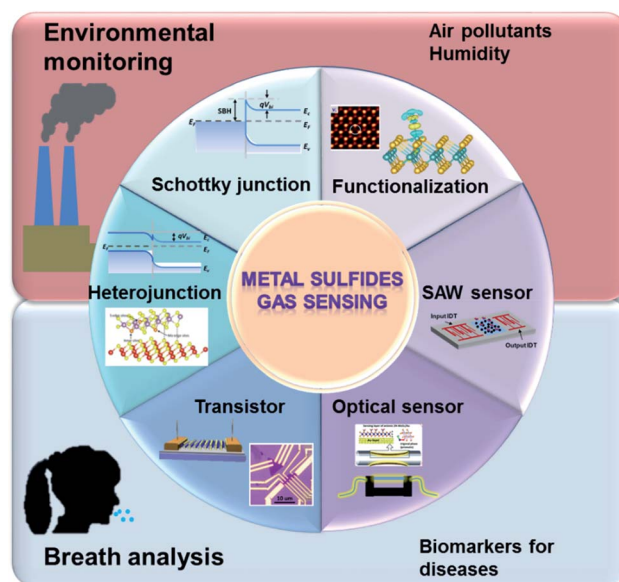
Fig. 2 Strategies of high-performance metal sulfide-based gas sensors and their applications. The heterojunction image is reprinted with permission from ref. 35 Copyright 2017, ACS Publishing. The functionalization images are reprinted with permission from ref. 36. Copyright 2013, ACS Publishing and reprinted with permission from ref. 37. Copyright 2017, Elsevier. The transistor image is reprinted with permission from ref. 38. Copyright 2013, ACS Publishing. The optical sensor image is reprinted with permission from ref. 39. Copyright 2020, ACS Publishing.

24944 | J. Mater. Chem. A, 2020, **8**, 24943–24976

This journal is © The Royal Society of Chemistry 2020

Fig. 3 Periodic table with symbols indicating metal sulfide.

sensing behaviours.[28] They have the advantages of a shallow valence band, exposed active sites, and the quantum size effect. Typical metal sulfide semiconductors, such as molybdenum disulfide (MoS_2) and tungsten disulfide (WS_2), are layered metal disulfide materials, which consist of several S–metal–S layers attached *via* weak van der Waals (vdW) force. Sensor metal sulfide materials act as charge acceptors or donors. Because of the high-speed charge transfer and the high adsorption energy between it and gas molecules, metal disulfide has been widely used in gas sensing. The LOD of a MoS_2 NO_2 gas sensor is 20 ppb.[29] For post-transition metal sulfide, tin sulfide (SnS) and germanium sulfide (GeS) are semiconductors that belong to a family of layered group IV monosulfides and have similar puckered structures to black phosphorus (BP).[30–32] Owing to its anisotropic crystal structure, SnS has been employed for the detection of VOCs and toxic gases, such as acetone, alcohol, and NO_2.[33,34] Additionally, many advanced methods were proposed to improve their sensing properties, such as functionalizing metal sulfide (*e.g.*, with defects or dopants), constructing heterojunctions (Schottky junctions and p–n, n–n, and p–p heterojunctions), and using transistors, see Fig. 2.

The present review will provide a comprehensive perspective on metal sulfide-based gas sensors, including the crystal structure, gas sensing mechanisms, applications, and perspectives. The paper is organized as follows: Section 2 describes the basic characteristics of metal sulfide nanomaterials. Section 3 discusses various gas sensing mechanisms of different metal sulfides through density functional theory (DFT). Section 4 summarises different sensing concepts of gas sensors based on metal sulfides. Section 5 lists the gas sensing applications of metal sulfide-based devices. Section 6 discusses the challenges and perspectives of metal sulfide sensors. This review is conceptually self-contained and intended to serve as an informational resource to newcomers and experienced researchers on metal sulfide-based sensors.

2. Gas sensing mechanisms of metal sulfides

Sulfide is an inorganic sulfur anion with the chemical formula S^{2-} or a compound containing one or more S^{2-} ions.[40] Metal sulfide is a kind of combination of sulfur anions and metal/semi-metal cations in the form of M_xS_y ($x : y = 1 : 1$, $1 : 2$, $2 : 1$, $3 : 4$).[41] As shown in Fig. 3, metal monosulfides mostly correspond to group VIII, IB, IIB, IIIA, and IVA metals. The elements from group IVB–VIIB and Sn can be used to form metal disulfides.[42] Materials of the same composition with different crystal phases have different properties. 2H phase group VIB disulfides are usually semiconducting, while the corresponding 1T, 1T', and Td phase crystals are metallic. Group IVA disulfides, such as GeS_2 and SnS_2, are often semiconductors. MoS_2, WS_2, and SnS_2 are group VIB semiconductors, which have been used for transistors. Compared to other disulfides, group VIB disulfides exhibit high carrier mobility. Table 2 introduces the characteristics and applications of nanostructured metal sulfides. It is found that numerous metal sulfides possess several crystal phases, which can be controlled by altering the fabrication processes and external stimulations.[41,43,44] The preparation strategies for metal sulfides primarily comprise "top-down" and "bottom-up" methods. The top-down approaches include sputtering, electrospinning, lithography, mechanical exfoliation (ME), and liquid phase exfoliation (LPE). Bottom-up strategies are chemical vapour deposition (CVD), atomic layer deposition (ALD), spray pyrolysis, pulsed laser deposition/ablation, thermal deposition, hydrothermal synthesis, solvothermal synthesis, and the self-assembly method. All these methods have been proposed to prepare large scale, high yield, and low-cost metal sulfides in the form of 0D, 1D, 2D, and 3D structures. Chandrasekaran *et al.*[40] presented a comprehensive review on preparation technologies of metal sulfides; complementarily, in this review we primarily focus on gas sensing mechanisms and applications.

It is demonstrated that the gas molecules physically or chemically adsorb at the surface of the nanostructured materials through adsorption energy. The higher the adsorption energy the stronger the adsorption interaction between gas molecules and metal sulfides. First-principles simulation, that is DFT calculations using plane waves and pseudopotentials, has become an efficient method to evaluate the sensing performance of 2D/nano-materials. Because the behaviours of atoms during chemical bonding and the flow of electrons in materials can be calculated through DFT based on quantum

Table 2 Characteristics and applications of nanostructured metal sulfides[a]

	Crystal structure	Electric conductivity	Bandgap [eV]	Fabrication method	Application	Ref.
SnS	Orthorhombic	p-type	Indirect 1.1	PVD	Photodetectors, gas sensors	45
GaS	Hexagonal	Semiconductor	Indirect 2.52	LPE	Hydrogen evolution reaction	46
GeS	Orthorhombic	p-type	(Monolayer) indirect 2.34	Vapour deposition	High electron mobility	32
ZnS	Hexagonal	n-type	Direct 3.7	Hydrothermal	Gas sensors, optical sensors	47
CdS	Hexagonal	n-type	Direct 2.42	Spray pyrolysis	Solar cells, gas sensors	48
CuS	Hexagonal	p-type	Direct 2.5	Deposition	Solar cells, gas sensors	49
PbS	Hexagonal	n-type	Bulk 0.373 nm 1.30	Chemical bath deposition	Solar cells, photonics, gas sensors	50 and 51
NiS	Rhombohedral	p-type	0.5	Solventless, thermal decomposition	Photocatalysts	52
MoS$_2$	2H hexagonal 1T	(2H) semiconductor (1T) metal	(Bulk) indirect 1.29 (Monolayer) direct 1.8	CVD, ME	FETs, photodetectors, solar cells, photonics, supercapacitors	53 and 54
WS$_2$	2H hexagonal 1T	(2H) n-type (1T) metal	(Bulk) indirect 1.3 (Monolayer) direct 2.1	CVD, ME	FETs, photodetectors, gas sensors	55
SnS$_2$	4H hexagonal	n-type	(Bulk) indirect 2.308 (Monolayer) indirect 2.033	CVD, ME	FETs, photovoltaics, photodetectors	56
ZrS$_2$	1T rhombohedral	n-type	(Bulk) indirect 1.7	CVD	Photoconductivity	57
HfS$_2$	1T rhombohedral	Semiconductor	Indirect 2.0	ME	FETs, phototransistors	58
NbS$_2$	2H hexagonal	Metal	0.73	CVD	Superconductivity	59
TaS$_2$	1T rhombohedral 2H hexagonal	Metal	0.7	CVD	Photosensitivity, superconductivity	60
TiS$_3$	Monoclinic	n-type	Direct 1.13	ME, CVT	Photodetectors, gas sensors	61 and 62
ZrS$_3$	Monoclinic	n-type	Direct 2.56	CVT	Photodetectors	63
HfS$_3$	Monoclinic	Semiconductor	—	CVT	FETs, photodetectors	64
TaS$_3$	Orthorhombic	Metal	—	—	FETs, gas sensors	65
In$_2$S$_3$	Tetragonal	n-type	Direct 2.02	CVD	Photodetectors, gas sensors	66

[a] Physical vapour deposition (PVD), chemical vapour transport (CVT).

mechanics, it is much easier to understand the behaviour of systems at the atomic scale. This section discusses the major parameter calculated using DFT for evaluating sensing performance, the sensing mechanism of different metal sulfide materials, such as pristine, doped, defective, and heterojunction-based metal sulfides.

2.1 Performance parameters based on DFT results

First-principles calculations are performed to calculate the band structure, adsorption energy (E_a), charge transfer (ΔQ), bandgap (E_g), charge density difference (CDD), electron localization function (ELF), and density of states (DOS) of the gas molecule–metal sulfide system.

The E_a of gas molecules on a substrate can be calculated as,

$$E_a = E_{\text{bare system}} + E_{\text{gases}} - E_{\text{total system}} \quad (1)$$

where $E_{\text{bare system}}$, E_{gases}, and $E_{\text{total system}}$ are the total energies of the optimized bare metal sulfide, isolated gas molecules, and metal sulfide + gas molecule system, respectively. A negative value of E_a indicates that the adsorption is exothermic. The

higher the E_a, the stronger the interaction between gas molecules and metal sulfides; E_a has a great influence on the sensitivity/response of the chemiresistive gas sensor. Usually, the selectivity of materials can be determined through the E_a among different types of gases, because the higher the E_a, the higher the probability of adsorption towards the specific gas. As shown in Fig. 4, the E_a of the H$_2$O/SnS system is relatively high (−0.388 eV) among the four types of gases in air, which indicates that SnS has good sensitivity and specificity for the detection of H$_2$O in air.

In addition to E_a, the electron transport property changes should also be considered. Charge transfer (ΔQ) is the total charge in the adsorbed gas molecule. It is shown as charge difference after DFT calculation, which can be calculated as follows:

$$\Delta Q = Q_{\text{total system}} - Q_{\text{bare system}} - Q_{\text{gases}} \quad (2)$$

where $Q_{\text{total system}}$, $Q_{\text{bare system}}$, and Q_{gases} are the total charge on metal sulfide + gases, metal sulfide, and gas molecules, respectively. The amount of charge transferred was calculated
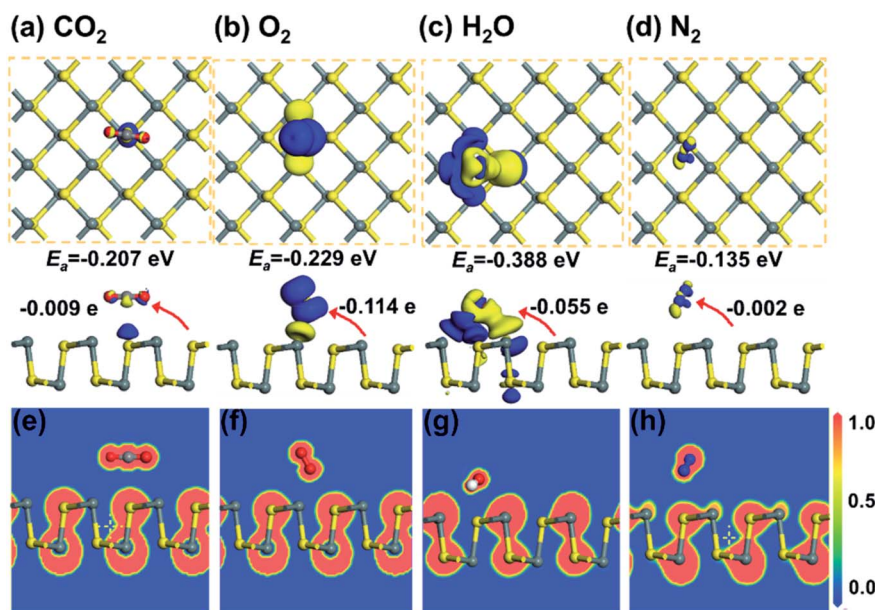
24946 | J. Mater. Chem. A, 2020, **8**, 24943–24976

This journal is © The Royal Society of Chemistry 2020

Fig. 4 The CDD for (a) CO_2, (b) O_2, (c) H_2O, and (d) N_2 adsorbed on monolayer SnS. The isosurface is taken as 0.003 e Å^{-3}. (e)–(h) show the corresponding ELF plots. Reprinted with permission from ref. 71. Copyright 2019, © IOP Publishing. All rights reserved.

by Löwdin analysis.[67] Some typical CDD images are shown in Fig. 4a–d. The blue region represents charge accumulation, while the yellow region shows charge depletion. These four types of gas molecule (CO_2, O_2, H_2O, and N_2) act as charge acceptors and receive electrons of 0.009e, 0.114e, 0.055e, and 0.002e from SnS, respectively.

In quantum chemistry, ELF is a measure of the possibility of finding an electron in the neighborhood space of a reference electron at a given point and with the same spin.[68] The ELF provides a method for mapping the electron pair probability in multielectronic systems and a description of electron delocalization in molecules and solids.[69] It can be used to analyze the extent of spatial localization of the reference electron and classify the chemical bond for almost all classes of compounds.[70] The ELF plots are normalized and present as

a jellium-like homogeneous electron. The normalized values of 1.00, 0.50, and 0.00 refer to fully localized electrons, fully delocalized electrons, and very low charge density, respectively. Some typical ELF images are shown in Fig. 4e–h. It is found that there is no remarkable electron sharing between gas molecules and SnS, which indicates that the chemical bond is unformed.

The DOS of a system presents the features of the electronic structure, such as the bandgap in insulators and the width of the valence band. It helps to qualitatively analyze the effects of external stimulations on the electronic structure, such as molecules, pressure, mechanical strain, and electric field. Fig. 5a shows the total DOS of the adsorption system of SnS without and with NH_3. The DOS of the SnS system changes slightly after adsorbing NH_3 molecules, which is associated with the electronic level
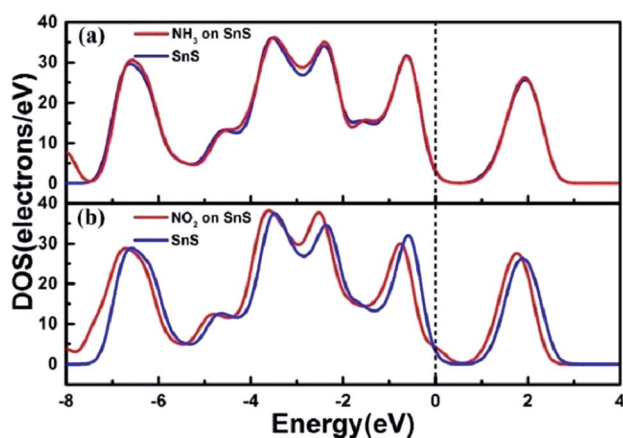

Fig. 5 The total DOS for (a) NH_3 and (b) NO_2 adsorbed on monolayer SnS. The Fermi level is set as zero. Reprinted with permission from ref. 72. Copyright 2017, IEEE.
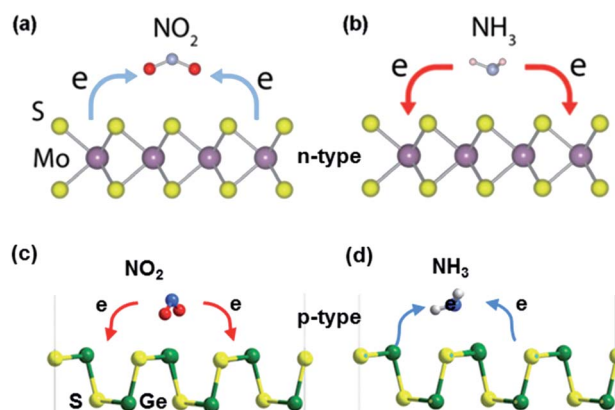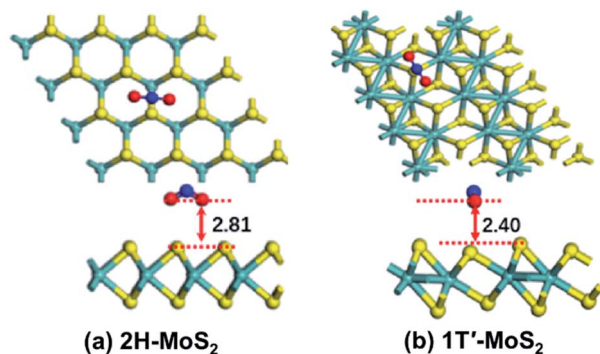

Fig. 6 Gas sensing mechanism of (a and b) MoS_2 (n-type metal sulfide). Reprinted with permission from ref. 27. Copyright 2018, ACS Publishing. (c and d) GeS (p-type metal sulfide) in the presence of NO_2 and NH_3 molecules. Reprinted with permission from ref. 77. Copyright 2018, The Royal Society of Chemistry.

Adsorption Energies (eV) of Gas Molecules on Both 2H- and 1T′-MoS2 Monolayers

MoS$_2$	CO	CO$_2$	NH$_3$	SO$_2$	NO	NO$_2$
2H	−0.14	−0.31	−0.18	−0.30	−0.16	−0.21
1T′	−0.15	−0.22	−0.22	−0.35	−0.47	−0.25

Fig. 7 Top and side view of the most stable configurations of NO$_2$ molecules adsorbed on (a) 2H−MoS$_2$ and (b) 1T′-MoS$_2$. The distance (Å) between the molecule (the lowest atom) and the MoS$_2$ sheets (the plane of the uppermost S atoms) is labelled. The bottom table shows the E_a of different gases on the 2H−MoS$_2$ and 1T′-MoS$_2$ monolayer. Reprinted with permission from ref. 79. Copyright 2019, ACS Publishing.

Fig. 9 The schematic of the interfacial interaction between the surface and interlayer of WS$_2$ and NH$_3$ molecules. Reprinted with permission from ref. 81. Copyright 2017, Elsevier.

localized between −4 eV and −2 eV in the valence band. However, concerning the NO$_2$/SnS system, there are obvious changes of the DOS on both sides near the Fermi level, which reveals the strong interaction between NO$_2$ and SnS (Fig. 5b).

2.2 Gas sensing mechanisms

2.2.1 Pristine metal sulfides

N-type and p-type metal sulfides. When exposed to gases, the charge transfer reaction occurs between the sensing materials and the adsorbed gases, accompanied by different transfer directions and 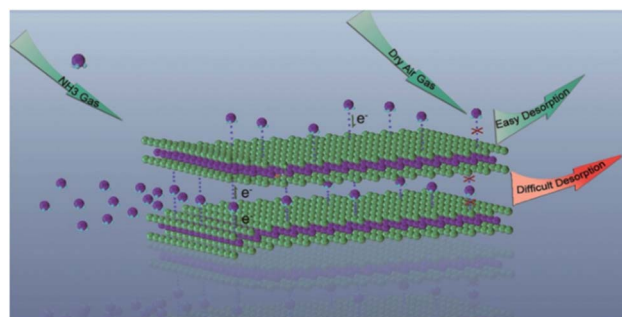quantities of charges, which leads to different changes in the material resistance. If the sensing materials are re-exposed to air, desorption of gas molecules occurs, causing the sensing material resistance to return to its initial state.[73] As shown in Fig. 6, when n-type MoS$_2$ is exposed to oxidizing gases such as O$_2$, H$_2$O, NO, NO$_2$, and CO, the electron charges transfer from MoS$_2$ to the sensitive gases, leading to a decreased carrier density in MoS$_2$. As a result, the resistance of n-type MoS$_2$ increases. In contrast, reducing (NH$_3$) gas molecules adsorbed on MoS$_2$ act as charge donors and transfer electrons to the MoS$_2$ monolayer, increasing the electron carrier density of the n-type MoS$_2$ monolayer and reducing its resistance.[74] Among post-transition metal sulfides, GeS is a p-type semiconductor, where the electron-accepting gases act as charge donors to GeS and NH$_3$ molecules trap electrons from GeS. Besides, lots of DFT calculations proved that gas molecules adsorb more strongly at the edge sites than at the basal plane of metal sulfides.[75,76]

2H and 1T′ phase of metal sulfides. 2H phase group VIB metal disulfides are usually semiconducting, and the corresponding

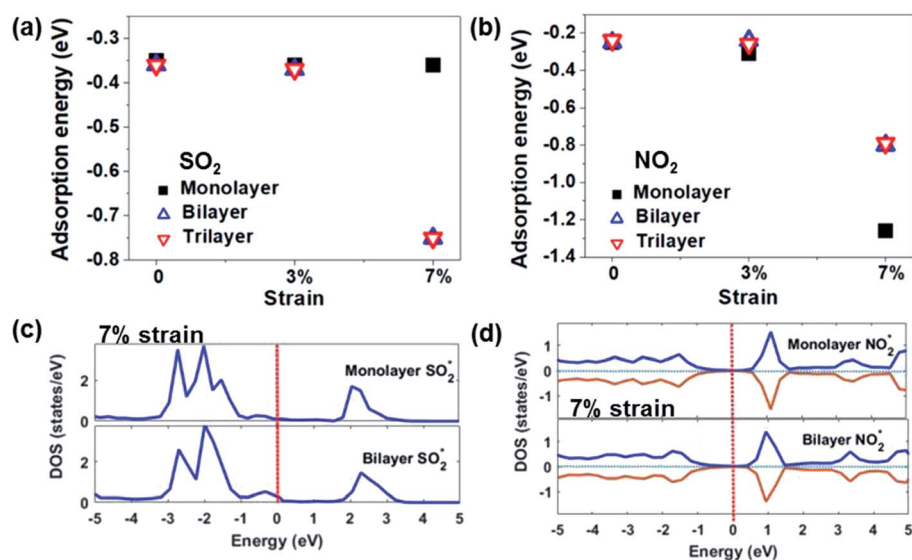Fig. 8 Adsorption energies of (a) SO$_2$ and (b) NO$_2$ on 1T′-MoS$_2$ sheets with a different number of layers and different strains. Total DOS of MoS$_2$ monolayer and bilayer systems at 7% strain adsorbed by (c) SO$_2$ and (d) NO$_2$. Reprinted with permission from ref. 79. Copyright 2019, ACS Publishing.

24948 | J. Mater. Chem. A, 2020, 8, 24943–24976

This journal is © The Royal Society of Chemistry 2020

1T, 1T′, and Td phase crystals are metallic. Different phases of metal sulfides have different E_a of the gas molecules over the sensor's surface. Putungan et al.[78] demonstrated that 1T′-MS$_2$ (M = Mo, W) are more stable than their 1T phases, ideal candidates for hydrogen evolution reaction (HER) catalysts. Linghu et al.[79] proved that the H adsorption strength on the basal plane of 1T′-MoS$_2$ is approximately 1.5 eV higher than that of 2H–MoS$_2$ because the molecules are closer to the 1T′-MoS$_2$ surface, allowing closer and stronger interaction. Besides, the 1T′-MoS$_2$-based sensors have higher E_a towards gas molecules (i.e., CO$_x$, NH$_3$, SO$_2$, and NO$_x$) than the sensors of 2H–MoS$_2$. The table in Fig. 7 reveals that 1T′-MoS$_2$ has high sensitivity and selectivity toward NO gas molecules. Tang et al.[80] compared and analyzed the stability and band-gap state of the 2H phase and 1T phase MoS$_2$ by covalent functionalization with H, CH$_3$, CF$_3$, OCH$_3$, and NH$_2$. The results showed that the chemical bonding is strong in the 1T phase but very weak in the 2H phase, associated with the metallicity and partially filled Mo 4d states of 1T-MoS$_2$.

The effects of the number of layers. It is well known that the number of layers affects the electronic properties of 2D materials. Based on the experimental results, it is found that multi-layer or few-layer MoS$_2$ was more stable and showed better gas sensing performance than its monolayer counterpart.[82,83] Concerning the DFT analysis results, Linghu et al.[79] investigated the

adsorption behaviour of SO$_2$, NH$_3$, NO, and NO$_2$ on bilayered and trilayered 1T′-MoS$_2$ sheets, as shown in Fig. 8. The 1T′-MoS$_2$ sheets with different thickness show only an approximately 0.01 eV change from the monolayer sheets without external mechanical strain. After applying 7% strain, the E_a of the tri-layered system changes significantly compared to that of the monolayer systems. This is associated with the new hybridized states or the occupied states of the gases near the Fermi level. Furthermore, the number of layers influences the recovery time of the devices. Qin et al.[81] found that the recovery time after detecting NH$_3$ has an anti-linear relationship with the number of layers. According to their DFT calculation results, the E_a of the NH$_3$ molecule intercalated into the interlayer of WS$_2$ (−0.356 eV) is higher than that of surface desorption (−0.179 eV), as shown in Fig. 9. The ratio of intercalated NH$_3$ to surface-adsorbed NH$_3$ becomes larger as the layer number increases. Therefore, the more the layers of WS$_2$, the longer the recovery time that is needed.

2.2.2 Doped metal sulfides. Chemical doping is an efficient way to change the band structure, modify the electronic and transport properties, and enhance the gas sensing applications. Metal doping is the most common method used for metal sulfides. Fig. 10 shows that typically doped metal atoms (i.e., V, Nb, and Ta) replace the Mo atoms of metal sulfides. Table 3 lists the different types of metal dopants for monolayer MoS$_2$, such
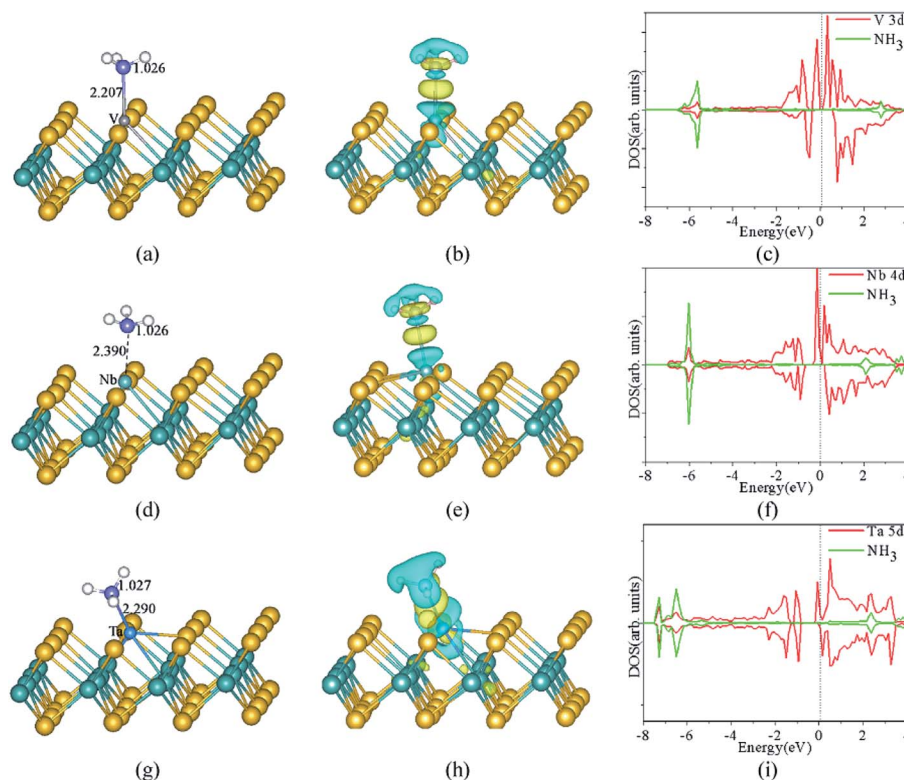
Fig. 10 The optimized structures, CDD, and corresponding spin-polarized DOS projected on 3d states of V atoms, adsorbed gas molecules of NH$_3$ adsorbed on the monolayer MoS$_2$ with V (a, b and c), Nb (d, e and f), and Ta (g, h and i) doped in the S-vacancy, respectively. The Mo, S, N, H, V, Nb, and Ta atoms are denoted by dark green, yellow, purple, white, light grey, light green, and blue spheres, respectively. The yellow and cyan regions represent the positive (electron accumulation) and negative (electron depletion) values, respectively. The isosurface value is taken as 0.003 e Å^{-3}. The vertical dashed line indicates the position of the Fermi level, taken as zero energy. Reprinted with permission from ref. 37. Copyright 2017, Elsevier.

This journal is © The Royal Society of Chemistry 2020

J. Mater. Chem. A, 2020, **8**, 24943–24976 | **24949**

Table 3 Literature study on the E_a of doped metal sulfide nanomaterials with different gas molecules

Material	Type of doping	NO$_2$	NO	CO	NH$_3$	SO$_2$	H$_2$S	SF$_6$	O$_2$	H$_2$	COF$_2$	CF$_4$	H$_2$O	Ref.
MoS$_2$	Pristine	−0.069	—	—	−0.063	—	—	—	—	—	—	—	—	85
	Al-doped	−3.02	—	—	−2.116	—	—	—	—	—	—	—	—	
	Si-doped	−2.588	—	—	−2.156	—	—	—	—	—	—	—	—	
	P-doped	−2.134	—	—	−0.34	—	—	—	—	—	—	—	—	
	Ni-doped	—	—	—	—	−1.382	−1.319	−0.181	—	—	—	—	—	86
	Ni-doped	—	—	—	—	—	—	—	—	—	0.723	0.265	—	84
	Pristine	—	0.11	0.07	—	—	—	—	—	—	—	—	—	87
	Cu-doped	—	1.25	1.44	—	—	—	—	—	—	—	—	—	
	Au-doped	—	1.08	0.91	—	—	—	—	—	—	—	—	—	88
	Pt-doped	—	1.21	1.38	—	—	—	—	—	—	—	—	—	
	Pd-doped	—	0.93	0.96	—	—	—	—	—	—	—	—	—	
	Ni-doped	—	1.62	1.38	—	—	—	—	—	—	—	—	—	
	V-doped	3.08	—	1.39	1.54	—	—	—	—	—	—	—	1.12	37
	Nb-doped	4.30	—	1.46	1.43	—	—	—	—	—	—	—	0.99	
	Ta-doped	4.05	—	1.78	1.95	—	—	—	—	—	—	—	1.65	
	Pristine	—	—	—	—	−0.36	—	—	—	—	—	—	—	89
	B-doped	—	—	—	—	−1.17	—	—	—	—	—	—	—	
	N-doped	—	—	—	—	−0.58	—	—	—	—	—	—	—	
	P-doped	—	—	—	—	−0.51	—	—	—	—	—	—	—	
	Al-doped	—	—	—	—	−2.33	—	—	—	—	—	—	—	
	Pristine	—	—	—	—	−0.209	—	—	—	—	—	—	—	90
	Ni-doped	—	—	—	—	−0.835	—	—	—	—	—	—	—	
	Fe-doped	—	—	—	—	−0.218	—	—	—	—	—	—	—	
	Co-doped	—	—	—	—	−0.213	—	—	—	—	—	—	—	
	Au-doped	—	—	1.16	—	—	—	—	—	—	—	—	0.41	91
	Cu-doped	—	—	1.31	—	—	—	—	—	—	—	—	0.68	
	AuCu-doped	—	—	1.13	—	—	—	—	—	—	—	—	0.61	
	Au$_2$Cu$_2$-doped	—	—	1.25	—	—	—	—	—	—	—	—	0.71	
	Au$_3$Cu$_3$-doped	—	—	1.23	—	—	—	—	—	—	—	—	0.63	
WS$_2$	Pristine	—	0.25	0.21	—	—	—	—	0.22	—	—	—	0.23	92
		−0.354	−0.206	−0.127	−0.216	—	—	—	−0.213	−0.075	—	—	−0.229	93

as Al, Si, P, Ni, Cu, Au, Pt, Pd, V, Nb, Ta, B, N, Fe, Co, and Au$_x$Cu$_y$, and their E_a after adsorbing different gas molecules (NO$_x$, CO, NH$_3$, SO$_2$, H$_2$S, SF$_6$, O$_2$, H$_2$, carbonyl fluoride (COF$_2$), cobalt tetrafluoride (CF$_4$), and H$_2$O). Based on the DFT results of all the metal-doped MoS$_2$ listed in Table 3, Ta-doped MoS$_2$ has the highest E_a of 4.30 eV towards NO$_2$, 1.78 eV towards CO, and 1.65 eV towards H$_2$O; Si-doped MoS$_2$ shows a high E_a of 2.156 eV to NH$_3$; Al-doped MoS$_2$ shows an E_a of 2.33 to SO$_2$. Besides, Li et al.[84] demonstrated that Ni-doped MoS$_2$ has great potential for sensing applications in organic gas molecules, such as COF$_2$ and CF$_4$.

2.2.3 Defective metal sulfides. It is known that the MoS$_2$ monolayer exhibits naturally formed vacancies, such as S vacancies (V$_S$) and Mo vacancies (V$_{Mo}$), which have significant impacts on the gas sensing performance.[94–97] Zhao et al.[94] investigated various defects in monolayer MoS$_2$, including monosulfur vacancies (V$_S$), disulfur vacancies (V$_{S_2}$), Mo vacancies (V$_{Mo}$), a vacancy complex of Mo with three (V$_{MoS_3}$) or six (V$_{MoS_6}$) nearby sulfur vacancies, antisite defects where a Mo atom is substituting a sulfur atom (Mo$_S$) or an S2 column (Mo$_{S2}$), antisite defects where a sulfur atom (S$_{Mo}$) or S2 column (S2$_{Mo}$) substitutes a Mo, and an external Mo (Mo–In). They found that four types of defect systems were stable after geometry optimizations, as shown in Fig. 11. These are mono-sulfur vacancies (MoS$_2$–V$_S$), disulfur vacancies (MoS$_2$–V$_{S_2}$),

antisite defects (MoS$_2$–Mo$_S$), and external Mo atoms (MoS$_2$–Mo). The corresponding E_a values after adsorbing O$_2$ are −1.822, −1.687, −3.293, and −2.545 eV for MoS$_2$–V$_S$–O$_2$, MoS$_2$–V$_{S_2}$–O$_2$, MoS$_2$–Mo$_S$–O$_2$, and MoS$_2$–Mo–O$_2$, respectively. All of them are much stronger than that of pristine MoS$_2$ (−0.01 eV).
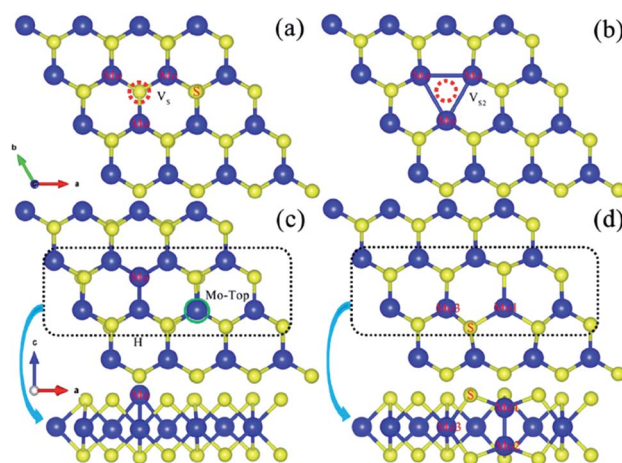

Fig. 11 Optimized geometric structure of the defect within a mono-layer MoS$_2$: (a) monosulfur vacancy (V$_S$), (b) disulfur vacancy (V$_{S_2}$), (c) antisite Mo$_S$, and (d) an external Mo located on the top of the Mo lattice site. Reprinted with permission from ref. 94. Copyright 2017, Elsevier.
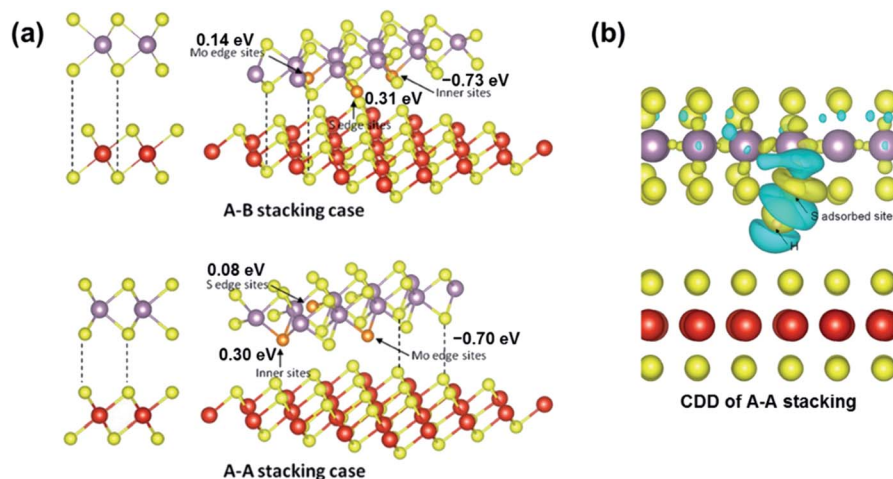
24950 | J. Mater. Chem. A, 2020, **8**, 24943–24976

This journal is © The Royal Society of Chemistry 2020

Fig. 12 (a) Two types of stacked bilayer structural models and their adsorption configurations. (b) CDD of the A–A stacking case (right) of the VS_2@MoS_2-edge nanosheet. The cyan and yellow regions represent the charge depletion and accumulation space, respectively. Reprinted with permission from ref. 35 Copyright 2017, ACS Publishing.

The CDD results reveal typical chemisorption of O_2 on the defective surface, which is associated with the O–O bond length extension in varying degrees.

2.2.4 Metal sulfide-based heterojunctions. Different stacking methods affect the E_a of the gas/substrate system. As shown in Fig. 12a, MoS_2/VS_2 heterojunctions with A–B and A–A stacking are built and used to investigate their hydrogen evolution ability.[35] The Gibbs free energies of the inner sites and Mo and S edge sites of the A–B and A–A stacking cases were also compared. The corresponding energies were calculated to be −0.73, 0.14, and 0.31 eV for the A–B stacking cases and −0.70, 0.08, and 0.30 eV for the A–A stacking cases. The difference of energies in these two stacking cases is associated with the bandgap barrier from VS_2 to MoS_2, which induces different internal charge transfer. The CDD image in Fig. 12b further proves the charge transfer between the adjacent H atoms and the S atom. There is still a lack of DFT simulation results of the gas molecule/heterojunction system for metal sulfides. Lots of experimental results are analyzed based on bandgap theory, which will be described in the next section.

3. Various sensing concepts of metal sulfide-based devices

Based on the gas sensing mechanism, metal sulfide-based devices can be classified into chemiresistors, Schottky junctions, heterojunctions, field-effect transistors (FETs), and optical and surface acoustic wave (SAW) gas sensors. In this section, we introduce the performance parameters as well as the sensing concepts of these devices.

3.1 Performance parameters

Typically, the criteria of an efficient gas sensor consist of high sensitivity and selectivity, fast response and recovery time, long-term stability, and low power consumption. Here, a set of parameters is defined to evaluate and compare the performance of different sensors, including response, sensitivity, selectivity, LOD, dynamic range, response and recovery time, and stability.

3.1.1 Response. The response is defined as the change in measured current (I), resistance (R), capacitance (C), conductance ($G = I/V$), light power (P), effective refractive index (RI), and resonant frequency (f) for a given gas concentration unit concerning the signal in the absence of analyte molecules. It is defined as:

$$(X_{gas} - X_0)/X_0 = \Delta X/X_0 \tag{3}$$

where $X = I$, R, C, G, P, RI, or f, X_{gas} is the sensor's signal after adsorbing the analyte gas, and X_0 is the baseline signal (no analyte gas). Different concentrations of the analyte gas could induce different responses. This review uses response in percentage (response%) = response × 100% to present the change of the testing signal.

3.1.2 Sensitivity. Sensitivity is defined as the capability to discriminate small differences in concentration or mass of the analyte. In other words, the sensitivity of the sensor is the slope of the calibration graph, which represents the variation in the sensor response per unit concentration of the target gas. In other words, sensitivity (S) = response/concentration. Thus, a higher sensitivity indicates a higher efficiency of the sensor.

3.1.3 Selectivity. Selectivity refers to the strong adsorption of target gases in the mixed gas, while being insensitive to other gases. The selectivity factor/coefficient (K) of the 'target gas' to another gas is defined as:

$$K = S_1/S_2 \tag{4}$$

where S_1 and S_2 are the sensitivities of the sensor to a target gas and another gas, respectively.

LOD is a key figure of merit in chemical sensing, used as an indicator of the minimum concentration of a detectable analyte.[98] Traditionally, LOD formulas, according to the International Union of Pure and Applied Chemistry (IUPAC), are based

This journal is © The Royal Society of Chemistry 2020

J. Mater. Chem. A, 2020, **8**, 24943–24976 | **24951**

on the use of linear regression models.[98] When the signal is three times greater than the noise, the theoretical LOD can be calculated from the slope of the linear region of the response curve, namely "Sensitivity (S)" and the root-mean-square (RMS) deviation at the baseline,

$$LOD = 3 \times RMS_{noise}/S \qquad (5)$$

where RMS_{noise} is the noise level in the absence of the analyte gas. Concerning the LOD in non-linear gas sensors, including metal oxide sensors, gas FETs, or thermoelectric sensors, Burgués *et al.*[99] proposed a methodology to estimate LOD through linearized calibration models.

Operating temperature (OT) is the temperature that corresponds to maximum sensitivity.

3.1.4 Response and recovery time. The response time (τ_s) and recovery time (τ_r) are defined as the time required for reaching 90% of the final response and the time taken to recover 90% of the original value of the device. They are mostly used as an index of the speed of response, which is highly dependent on the types of gases, the device structure, and the exposure time.

Stability is defined as the ability of a sensor to provide consistent and reproducible results for a specified period. This parameter becomes highly important when sensors are exposed to hazardous, corrosive, or high-temperature atmospheres.

Usually, an ideal gas sensor would possess high sensitivity, selectivity and stability, low LOD, and short recovery and response times. But its final application depends on the requirements of the specified environment or working conditions. Moreover, all the parameters could be affected by other factors, including the sensing materials, substrate, environmental factors (temperature, humidity, and pressure), and testing setup (volume, shape, and gas flow rate).

3.2 Chemiresistor gas sensors

Typically, different types of metal sulfides, such as nanoflakes (NFKs), nanosheets (NSs), nanowires (NWs), nanorods (NRs), nanoflowers (NFWs), or nanotubes (NTs), are synthesized or transferred on a substrate (*i.e.*, sapphire, Si, and SiC) to form a chemiresistor sensor, as shown in Fig. 13. The electrodes can be pre-made on the substrate or evaporated on the top of metal sulfides after the transfer process.

As mentioned in Section 2.2, the basic sensing principle is metal sulfides act as charge acceptors or donors. Their shallow valence band, small effective mass, and diverse structures enable a quantum size effect and promising applications in gas
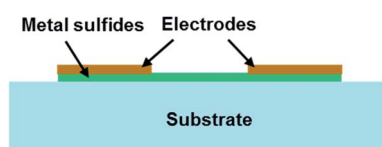

Fig. 13 Schematic of the structure of a metal sulfide-based chemiresistor gas sensor.

sensing. The typical direct narrow bandgap IV–VI compound semiconductors, such as SnS, PbS, and GeS, have similar puckered structures to black phosphorus.[30,31] They have been employed for the detection of toxic (NO_2, NH_3, and H_2S) and organic (*e.g.*, acetone and ethanol) gas molecules. The response and recovery time is fast (5–36 s).[33,100,101] The II–VI compound semiconductors mostly have a direct wide bandgap, including CdS and ZnS. They have high response and selectivity to VOCs, including isopropanol, methanol, ethanol, acetone, and methylbenzene. However, their OTs are relatively high (200–300 °C).[102,103] Other metal monosulfide-based gas sensors, such as CuS and NiS, also have potential applications in H_2 and SO_2 gas sensing.[104–106] According to Kim's research, 75% of publications up to 2017 were focused on MoS_2 followed by WS_2 (14%) and SnS_2 (9%).[13] The predominance of MoS_2 over other metal disulfides is because this material is the easiest to synthesize and the most stable among transition metal sulfides. Most transition metal sulfides are composed of metal atoms sandwiched between two layers of hexagonally close-packed sulfur (S) atoms; the adjacent S layers are connected by the weak van der Waals forces. They have a larger electronegativity, potentially increasing the number of gas adsorption sites. Thus various transition metal sulfides, including NbS_2, ReS_2, TaS_2, and VS_2, were used for gas sensing in NO_x, NH_3, O_2, and ethanol.

Functionalization is a versatile method for the modulation of the electronic and chemical properties of metal sulfides. As discussed in Section 2.2, doping and defect substitution are the most commonly used tools in functionalization, which can change the electronic structure, modify chemical reactivity, and affect the sensing performance.[108] Fig. 14 shows a hydrogen sensor with few-layered Pd-doped MoS_2 and various point defects in CVD-MoS_2.[36,107] Qin *et al.*[109] demonstrated an enhanced NH_3 sensor based on 2D SnS_2 with sulfur vacancies. It showed a fast response time of 16 s toward 500 ppm NH_3. The enhanced sensitivity is associated with the high E_a of the defective system of 2D SnS_2. However, most of the gas-sensing behaviours of functionalized metal sulfides were analyzed through DFT calculations. There are a lack of experimental reports on the influence of defects on the metal sulfide-based devices' gas-sensing performance.

3.3 Schottky junction

Typically, a metal–semiconductor (M–S) junction is a type of heterostructure where a metal is in close contact with a semiconductor material. The rectifying M–S junction is called a Schottky junction, while the non-rectifying junction forms an ohmic contact. Recently, researchers reported that a Schottky or an ohmic contact can also be formed between an atomic CNM and a semiconductor, depending on their electron affinity values.[8] Fig. 15a shows a typical Schottky junction, in which the electrons flow from the conduction band to the semiconductor layer until they reach equilibrium. This forms a Schottky barrier (SB) of the built-in potential barrier (V_{bi}) in the contact layer and hinders further charge transport.[110] The Schottky barrier height (SBH) from the metal side remains unchanged, while the bias
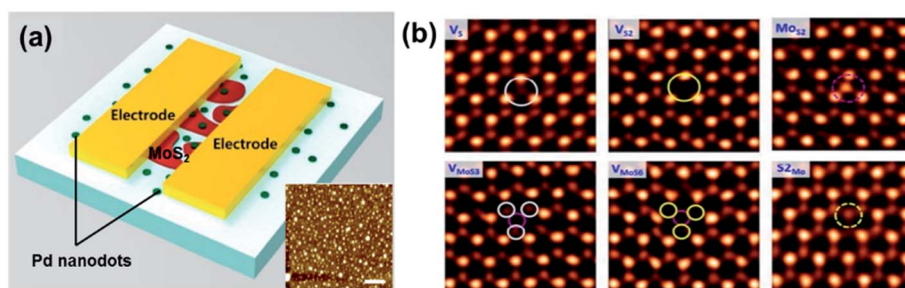
24952 | *J. Mater. Chem. A*, 2020, **8**, 24943–24976

This journal is © The Royal Society of Chemistry 2020

Fig. 14 (a) Schematic of a Pd-doped MoS$_2$-based sensor. The inset image shows the AFM image of Pd on a SiO$_2$ substrate. The scale bars indicate a distance of 400 nm. Reprinted with permission from ref. 107. Copyright 2017, Elsevier. (b) Image analysis for intrinsic point defects in ML MoS$_2$. Reprinted with permission from ref. 36. Copyright 2013, ACS Publishing.

across the junction could change according to the work function of the semiconductor (φ_s). As shown in Fig. 15b(i–v), the SBH was controlled using different metals (Au, Ag, and Al) as the materials of electrodes. The adsorbed gas molecules, i.e., CO$_x$, are a kind of dopant for the semiconductor, which could modify the doping level of materials and modulate the φ_s in turn (see Fig. 15b(iv and v)).[111] The SB is determined from the difference between φ_m and φ_s, strongly influenced by the gas molecules. Therefore, the SBH is easily varied owing to the change of the gas concentration. Fig. 15b(ii) shows that the response to CO gas is improved in devices after using the Ag electrode due to the increase in SBH, which means that the Schottky contact sensor could improve the sensitivity because the modulations of the φ_{B0} and barrier width in the Schottky junction by gas molecules are concentrated in the tiny area of contact between the metal and metal sulfides and the Schottky diode-based sensor can detect ultralow levels.[112,113] Besides, the sensing performances of vdW vertical heterojunctions of CNMs and

metal sulfides are not only associated with the SBH modulation mechanism but also with the abundant adsorption sites on the CNMs' surfaces. This enables a significant enhancement of the device sensitivity toward the ppb level of NO$_2$ gas exposure reaching 4.9%/ppb (4900%/ppm).[114]

3.4 Heterojunction based gas sensors

Heterojunctions based on metal sulfide can be easily constructed and present superior electric and photoelectric properties compared to pristine metal sulfide owing to the abundant adsorption sites and unique interface state at the contact interface.[115] According to the type of semiconductors, 2D heterojunctions can be classified as p–n, n–n, and p–p junctions.

3.4.1 p–n junction. The band alignment of a p–n heterojunction is shown in Fig. 16a; electrons and holes flow in opposite directions until equilibrium is achieved, forming a thick space-charge region that further narrows the electrical transport channels. Mostly, in p–n heterojunction gas sensors,
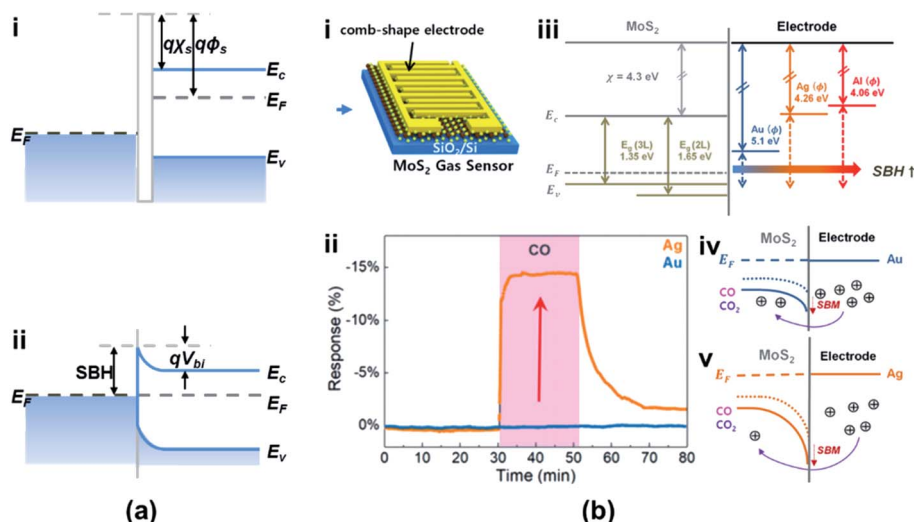

Fig. 15 Band alignment of (a) the Schottky junction. E_c, E_F, and E_v are the conduction band edge, Fermi level, and valence band edge of the semiconductor, respectively. φ_m, φ_s, and χ_s are the metal work function (measured in volts), the semiconductor work function, and electron affinity, respectively. φ_{B0}, V_{bi}, and x_n are the barrier height, built-in potential barrier, and depletion width, respectively. Other symbols have their usual meaning. (b) (i) Schematic of the metal-MoS$_2$ Schottky contact gas sensor. (ii) Sensing characteristics of CO for 2 L MoS$_2$ with Au and Ag electrodes. (iii) Band diagram of MoS$_2$ with metal electrodes. Band alignment of (iv) the Au/MoS$_2$ gas sensor and (v) Ag/MoS$_2$ gas sensor before and after CO and CO$_2$ exposure. Reprinted with permission from ref. 111. Copyright 2019, ACS Publishing.

This journal is © The Royal Society of Chemistry 2020

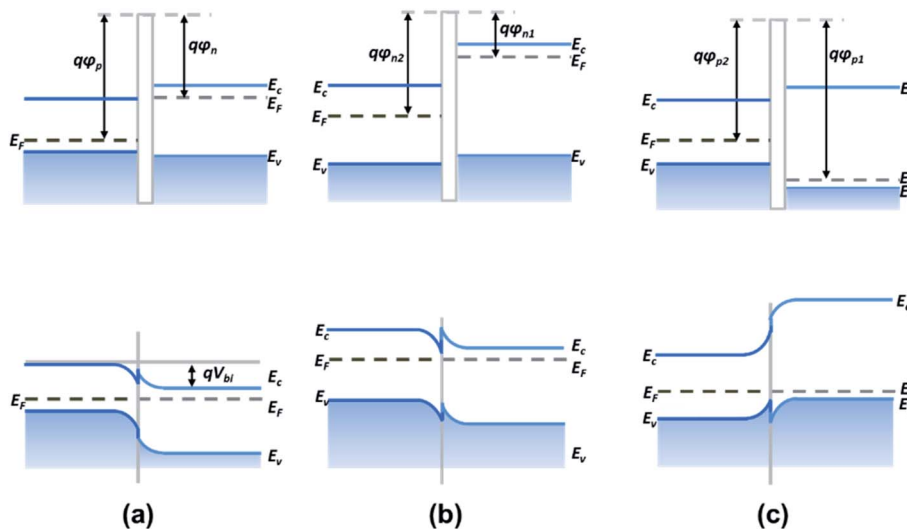J. Mater. Chem. A, 2020, **8**, 24943–24976 | **24953**

Fig. 16 Band alignment of (a) p–n junctions, (b) n–n junctions, and (c) p–p junctions. E_c, E_F, and E_v are the conduction band edge, Fermi level, and valence band edge of the semiconductor, respectively. φ_p, φ_n, and V_{bi} are the p-type semiconductor work function, the n-type semiconductor work function, and the built-in potential barrier, respectively.[116]

the sensing performances are determined by the difference in the areal coverage of the two dissimilar materials as well as the interfacial bonds.[41,117] With a higher areal coverage of the material, more electrons flow through the material, and so the charge transfer between gas molecules and the material is stronger than in the case of the material with lower areal coverage. Higher area materials dominate the sensing response of the p–n heterojunction. Concerning the interfacial states of a p–n junction, there are many dangling bonds and voids in the interface owing to a random connection between two different crystals.[118] Since dangling bonds could trap the electron in the conduction path, the charge transfer is impeded, requiring additional energy to drive the electrons across the electron-depletion layer (EDL). Therefore, it is recommended to keep the interface state at a low density, for instance, by adopting lattice-matched materials or enhancing the crystal quality of the materials. Through the hydrothermal method, MoS_2/SnO_2 p–n heterojunctions have been fabricated and used for ethanol, trimethylamine (TMA), and NO_2 gas sensing.[119–121] They exhibited high sensitivity, lower OT, excellent sensing selectivity, and outstanding long-term stability. However, there are still a lack of quantitative experimental and theoretical analyses of the effects of areal coverage and dangling bonds on the gas sensing performances.

3.4.2 n–n or p–p junction. Recently, various n–n and p–p heterostructures have been proposed to improve the gas-sensing performances. Most of the n–n and p–p junction gas sensors are based on metal oxide nanomaterials, such as SnO_2/TiO_2,[122] SnO_2/ZnO,[123] SnO_2/Sn_3O_4,[124] TiO_2/ZnO,[125] CaO/ZnO,[126] ZnO/In_2O_3,[127] and CuO/rGO,[128] whose enhanced performances are attributed to the heterocontact of the two semiconductor surfaces. For metal sulfide-based n–n and p–p heterojunctions, Zhang et al.[129] optimized the NH_3 sensing behaviour by using SnS_2/ZnS hierarchical NFWs. The gas sensors based on metal sulfide n–n junctions benefiting from metal oxide hybrids, such

as CdS/CeO_2,[130] CdS/ZnO,[131] ZnS/ZnO,[132] and ZnS/CuO[133] have been employed for the detection of VOC toxic gases. The electrons flow across the heterojunction from the higher Fermi level to the lower one, which induces band bending and EDL formation at the interface. This improves the transfer efficiency of the interfacial charge and increases the adsorption of oxygen species. An EDL and electron-accumulation layer (EAL) are formed at n–n (Fig. 16b) and p–p (Fig. 16c) heterointerfaces. The adsorbed gases on the surface could further influence the width of the EDL/EAL by extracting/giving electrons from/to the conduction band of the semiconductors. Therefore, the conductivity of the device could be altered with the type and the concentration of analytes (gas molecules). Moreover, the interface states of n–n or p–p heterojunctions need further experimental and theoretical analysis.

3.5 FET gas sensors

FET gas sensors have attracted much research interest because of their sensitive detection and miniaturization.[134,135] Fig. 17 shows a typical FET gas sensor consisting of a sensing semiconductor as a channel material, a back gate layer, a dielectric layer, and source and drain electrodes on the two ends of the channel material. The conductance of the channel can be modulated by applying different bias voltages on the gate electrode through a thin dielectric layer.[8] The channel materials could be pristine or functionalized metal sulfides and metal sulfide-based heterojunctions. Similarly to the chemiresistor gas sensor, gas detection can be realized by measuring the change of the current between the source and drain (I_{ds}) before and after exposure to target gases. The primary difference is that the gate voltage could alter the channel's charge carrier concentration by modulating the electric field across the dielectric layer. Consequently, the charge transfer between channel and target gases could be modified in the form of
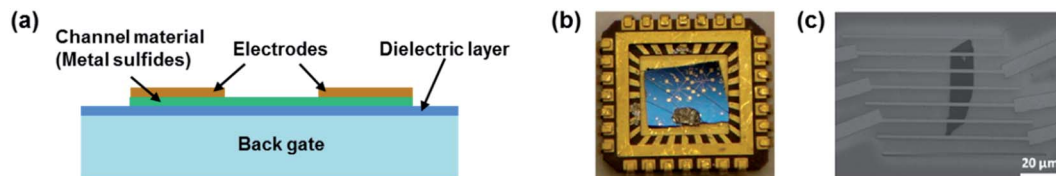
24954 | J. Mater. Chem. A, 2020, **8**, 24943–24976

This journal is © The Royal Society of Chemistry 2020

Fig. 17 (a) Schematic of an FET gas sensor. (b) Optical image of the MoS_2 transistor sensor on a chip. (c) SEM image of a two-layer MoS_2 transistor. Reprinted with permission from ref. 83. Copyright 2013, ACS Publishing.

changes in the I_{ds}. Traditionally, FET sensors could be back-gate FETs and top-gate FETs; however, most FET gas sensors are back-gate FETs because the channel materials can directly come into contact with target gases. This type of sensing device has been used to detect many types of gases, such as CO, NO, NH_3, NO_2, SO_2, H_2, and VOCs. However, most FET gas sensors are still not satisfactory due to their device instability and limited large-scale production even though they exhibit fast response and high selectivity.[136]

3.6 Optical gas sensors

Optical gas sensors monitor the optical properties of different gas species at defined optical wavelengths. They can be used as an optical "fingerprint" for any gas species because different types of gases have a specific distribution of optical absorption/emission with the wavelength. Besides, different changes in optical properties of sensors can reflect different gas concentrations. Metal sulfides have strong photoluminescence, a wide range of photoresponsivity, high carrier mobility, and high sensitivity to humidity variation.[4,40] Fibre-optic sensors are attractive due to their low cost, light weight, and anti-corrosion properties.[137] Therefore, taking advantage of the superior properties of both metal sulfides and optical fibres was considered. Most of metal sulfide-based optical gas sensors are fibre-optic devices. The MoS_2-coated side polished fibre (SPF) sensor has a high response, and the MoS_2-coated etched single-mode fibre (ESMF) has a fast response time, enabling the fibre-optic sensor to monitor different breathing patterns of human beings.[138] As shown in Fig. 18, the normalized response (NR) of the $2H$–MoS_2/Au coated optical fibre device was calculated from the change of the transmission light power, and the sensitivity

was determined using $S = \Delta NR/\Delta RH$, where ΔNR is the relative variation in the transmitted light intensity for the sensor and ΔRH is the change of relative humidity, respectively.[39]

3.7 SAW gas sensors

The SAW sensor is based on the microelectromechanical system (MEMS), which converts an input electrical signal into a SAW, *i.e.*, a mechanical wave.[139] Fig. 19 shows a typical SAW gas sensor structure, whose SAW delay line between the input and output interdigital-transducer (IDT) is covered by a thin membrane that can selectively adsorb the gas to be detected. Any change in phase, frequency, amplitude, or time-delay induced by gas adsorption or desorption of the membrane, might further affect the wave. Then it is converted into an electrical signal and received by the output end. In particular, the phase velocities can be detected with high accuracy. In this case, SnS colloidal quantum dots (CQDs) were used as the sensing layer and fabricated on the ST-cut quartz substrate.[140] The sensor exhibited high selectivity and efficiency for the detection of NO_2 gas with low concentration at room temperature. Moreover, this is an efficient approach to diagnose diseases from exhaled breath by coating SAW sensors with various polymers to identify specific breath biomarkers.

4. Metal sulfide-based devices for gas sensing applications

4.1 VOCs

VOCs primarily come from the exhaust gases generated by transportation, fuel combustion, and come from cooking, furniture, decorative materials, or much simpler breathing.[141]
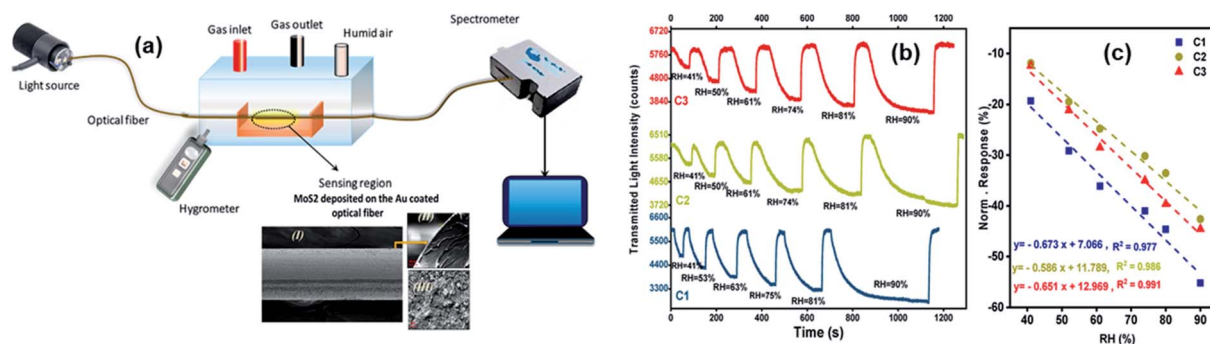
Fig. 18 (a) Schematic diagram of the gas sensing transmittance setup on the basis of an optical fiber coated with thin layers of anionic MoS_2 and Au. The inset image shows the cross-sectional FE-SEM images of the anionic $2H$–MoS_2/Au coated optical fibre. (b) Dynamic and (c) sensitivity responses of the optical fiber sensors modified with different samples. Reprinted with permission from ref. 39. Copyright 2020, ACS Publishing.

This journal is © The Royal Society of Chemistry 2020

J. Mater. Chem. A, 2020, **8**, 24943–24976 | **24955**

Fig. 19 (a) The schematic and (b) a photograph of the SAW sensor based on SnS CQDs. (c) The response curves of the SAW sensor to different NO_2 concentrations. (d) The dependence of the response on NO_2 concentration. Reprinted with permission from ref. 140. Copyright 2019, Elsevier.

Since the concentration of VOCs an indoor ambient environment is much higher than that outdoors (up to 10 times), the level of VOCs is used as one of the indicators for evaluating the air quality in indoor ambient.[98] When people are exposed to a certain concentration of VOCs, they face a higher risk of 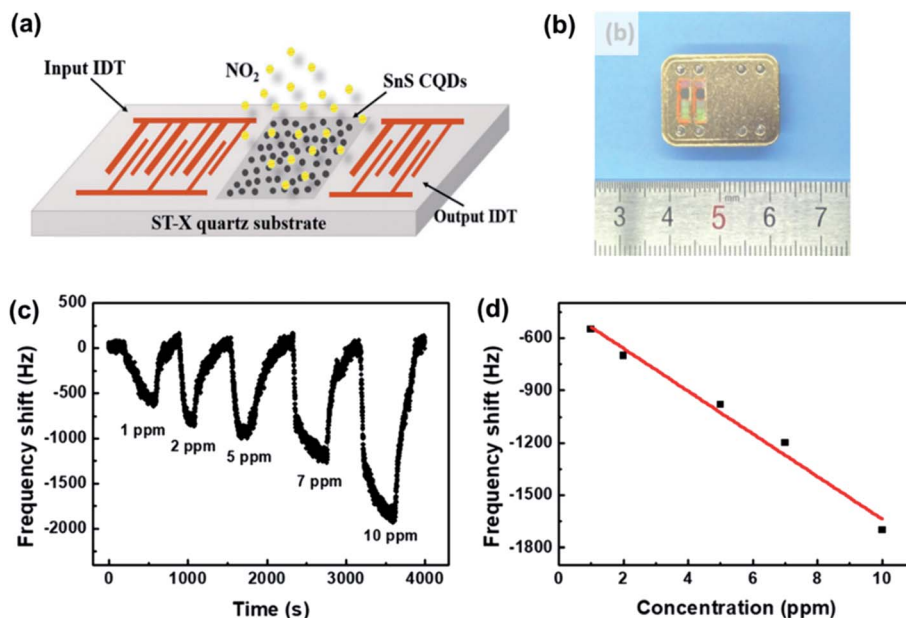suffering from headaches, nausea, and even organ damage. From a medical perspective, exhaled breath contains VOCs of alcohols, hydrocarbons, ketones, aldehydes, esters, nitriles, and aromatic compounds,[142,143] which can be used as biomarkers of the diagnosis of diseases according to Fig. 1. The gas-sensing performance of metal sulfide-based devices towards different VOCs is summarised in Tables 4–6.

4.1.1 Acetone. Acetone is one of the common metabolites of the human body and is ordinarily present in the breath, blood, and urine. Increased acetone in the breath can be found in untreated patients with diabetes mellitus.[144,145] Typically, the acetone concentration for diabetic patients is higher than 1.71 parts per million by volume (ppmv), whereas that for healthy people ranges from 0.3 to 0.9 ppmv.[146] The detection and analysis of acetone in the breath can be a potential method for the diagnosis of diabetes. Besides, acetone may also be associated with lung cancer.[142] To achieve high sensitivity, various shapes of metal sulfides were used. The SnS NFK-based gas sensor showed excellent stability and reproducibility at 100 °C for the detection of acetone from 5 to 50 ppm and a rapid response of 3 s.[34] Wang *et al.*[103] fabricated a single-crystal ZnS NW-based gas sensor through the thermal-evaporation-growth method, which showed high sensing selectivity towards acetone and ethanol. Giberti *et al.*[147] obtained SnS_2 NRs as a precipitate in aqueous solution and deposited them as functional materials on an alumina substrate for acetone, acetaldehyde, and H_2S gas sensing. The sensor showed excellent

selectivity to acetone at 1 ppm under both dry and wet conditions at an OT of 300 °C. To decrease the OT, SnS_2/SnO_2 heterojunctions were employed for the detection of acetone, and they showed a response% of 107% and fast recovery (80 s) at 80 °C.[148] However, the LOD could not meet the limit of acetone concentration in the exhaled breath (0.9 ppm), which shows that the LOD of metal sulfide-based gas sensors needs to be improved further.

4.1.2 Benzene. Benzene gas is volatile and highly toxic; even a small amount of benzene can cause vital harm to our body.[149] The maximum permitted exposure limit in the atmosphere regulated by the World Health Organization (WHO) is 5 ppb (16.25 μg m^{-3}).[150] However, benzene is commonly used as a solvent in petrochemical and pharmaceutical goods, which has terrible carcinogenic effects on the people working there. It is necessary to detect-trace benzene in the environment, which has led to the development of inexpensive sensors for benzene detection. The conventional methods are based on cataluminescence, chromatography, and spectroscopy.[149,151,152] Recently, semiconductor sensors were explored. For metal sulfide-based devices, Zhang *et al.*[153] synthesized and used Pd-decorated TiO_2/MoS_2 ternary nanocomposites in the benzene sensor. Compared to pristine MoS_2 and TiO_2 sensors, this sensor has a higher response% of 64% for 50 ppm benzene, wider linearity ranging from 0.1 to 100 ppm, shorter response and recovery times (13 s/10 s), and better selectivity and stability. Moreover, this group employed WS_2 NFWs/ZnO hollow spheres to detect benzene, which showed a faster response and recovery time of 8 s/6 s at room temperature.[154] To extend the application area, Baek *et al.*[155] demonstrated a flexible and transparent benzene sensor using cobalt-metalloporphyrin (Co-MPP)-functionalized few-layer MoS_2 as the sensing material.

24956 | *J. Mater. Chem. A*, 2020, **8**, 24943–24976

This journal is © The Royal Society of Chemistry 2020

Table 4 Literature study on the gas-sensing performance of metal sulfide-based VOC gas sensors[a]

Material	Structure	Synthesis method	Analyte	Concentration (ppm)	Response (%)	LOD (ppm)	τ_s/τ_r	OT (°C)	Ref.
SnS	NFKs	Solid state reaction	Acetone	20	1000	—	3 s/14 s	100	34
ZnS	NWs	Thermal evaporation	Acetone	100	2120	0.5	10 s/7 s	320	103
MoS_2	Nanofilm	ME	Acetone	5000	~1.2	500	—	RT	38
SnS_2	NRs	Precipitation in aqueous solution	Acetone	10	~2500 (dry) ~210 (17% RH)	1	—	300	147
$Pd–TiO_2/MoS_2$	Nanocomposites	Hydrothermal method	Benzene	50	64	0.1	13 s/10 s	RT	153
ZnO/MoS_2	p–n junction	Screen printing	Benzene	20	30	0.1	8 s/6 s	RT	154
Co-MPP-functionalized MoS_2	Nanocomposites	Solvent mixing	Benzene	10	22	—	~500 s/ ~100 s	RT	155
PbS	NSs	Chemical reaction	Methane	10 000	~10	—	—	RT	159
Au NPs/PbS	Nanocomposites	Chemical reaction	Methane	30 000	30	—	180 s/70 s	RT	160
Ag NPs/PbS	Nanocomposites	Chemical reaction	Methane	80 000	35	—	60 s/150 s	RT	161
PbS NCs/rGO	Nanocomposites	Chemical reaction & hydrothermal method	Methane	10 000	45	—	90 s/65 s	RT	162
$ZnS:Mn^{2+}$ (optical)	QDs	Chemical precipitation	Methane	100	~50*	—	—	RT	164
SnO_2/MoS_2	Nanocomposites	Electrospinning and hydrothermal method	Methane	100	101.4*	—	150 s/20 s	180	163
ZnS	0D nanosphere	Hydrothermal method	Formaldehyde	50	9440*	—	11 s/8 s	295	165
rGO/MoS_2	Hybrid films	Layer-by-layer (LBL) self-assembly	Formaldehyde	10	2.8	—	—	RT	166
In_2O_3/MoS_2	Nanocubes/nanofilm	LBL self-assembly	Formaldehyde	50	75.2	0.2	14 s/22 s	RT	167
In_2O_3/WS_2	Nanocomposites	LBL self-assembly	Formaldehyde	5	7.5	—	98 s/137 s	RT	168
Ni-doped In_2O_3/WS_2	Nanocomposites	LBL self-assembly	Formaldehyde	20	32	0.015	76 s/123 s	RT	

[a] * means the response% is recalculated as $(X_{gas} − X_0)/X_0 = \Delta X/X_0$ in this review. In the original reference, the response (%) is defined as X_{gas}/X_{air}.

The device has a higher response% of over 250% compared to pristine MoS_2 and a low LOD of 10 ppm at room temperature.

4.1.3 Methane. Methane (CH_4) is widely present in industrial and residential areas and emitted into the atmosphere from natural wetlands, rice paddies, domestic ruminants, landfills, and biomass burning.[156] It is a potent greenhouse gas, whose explosive limit concentration was reported to be more than 4.7% mixed with air.[157] Traditionally, exhaled air from normal human breath doesn't have methane, except in people who are overweight and people who have irritable bowel syndrome, inflammatory bowel diseases, or anorexia.[158] Taking advantage of the nanostructures, metal sulfide nanocrystals (NCs) and quantum dots (QDs) have been used in CH_4 sensors. Sheikhi et al. proposed a series of PbS-based chemiresistor sensors for the detection of CH_4, including intrinsic PbS NCs,[159] Au nanoparticle (NP) decorated PbS,[160] Ag NP decorated PbS,[161] and PbS NCs/rGO hybrids.[162] The PbS NCs/rGO nanocomposite sensor has shown a good response% (45%) at the lower explosive limit of CH_4 with fast response and recovery time (90 s/65 s). Wang et al. employed hierarchical nanocomposites of MoS_2 NFWs anchored on SnO_2 nanofibers for CH_4 sensing. As shown in Fig. 20, this n–n junction-based sensor showed a high response% of 101.4% toward 100 ppm CH_4 at 180 °C.[163] With respect to optical gas sensors, Sergeev et al.[164] synthesized manganese-doped zinc sulfide ($ZnS:Mn^{2+}$) QDs and found that the $ZnS:Mn^{2+}$ emission spectrum is changed significantly under exposure to CH_4 in the concentration range from 100 ppm to

2000 ppm. QDs in this luminescent sensor act as adsorption centres for achieving higher light transmittance and further improving the signal stability in the visible region. The response refers to the photoinduced electron transfer from QDs to CH_4, which induces QD luminescence quenching and a decrease in the luminescence lifetime.

4.1.4 Formaldehyde. Formaldehyde (HCHO) is a colorless toxic gas with a pungent smell and can cause serious harm to the central nervous system and immune system of human beings. Because formaldehyde is a chemical used in the production of solvents, adhesives, and bonding agents, it is usually released from pressed-wood products, wallpapers, paints, and foam insulation in homes, offices, and the urban environment. According to the Occupational Safety and Health Standards, the time-weighted average limit of formaldehyde is 0.75 ppm, the short-term exposure limit is 2 ppm and the immediately dangerous to life or health limit is 20 ppm.[169] In the view of healthcare, HCHO could act as a biomarker of multiple diseases, especially lung cancer.[150]

Hussain et al.[165] successfully prepared 0D ZnS nanospheres via a low-temperature hydrothermal synthesis method. The gas sensor showed a high response% of 9540% and high selectivity towards formaldehyde compared to other gases (ethanol, ammonia, acetone, methanol, and NO_2) at an OT of 295 °C. The enhanced gas-sensing performances can be attributed to the presence of more active sites because of the large exposed surface area and small size of ZnS nanospheres. Li et al.[166]
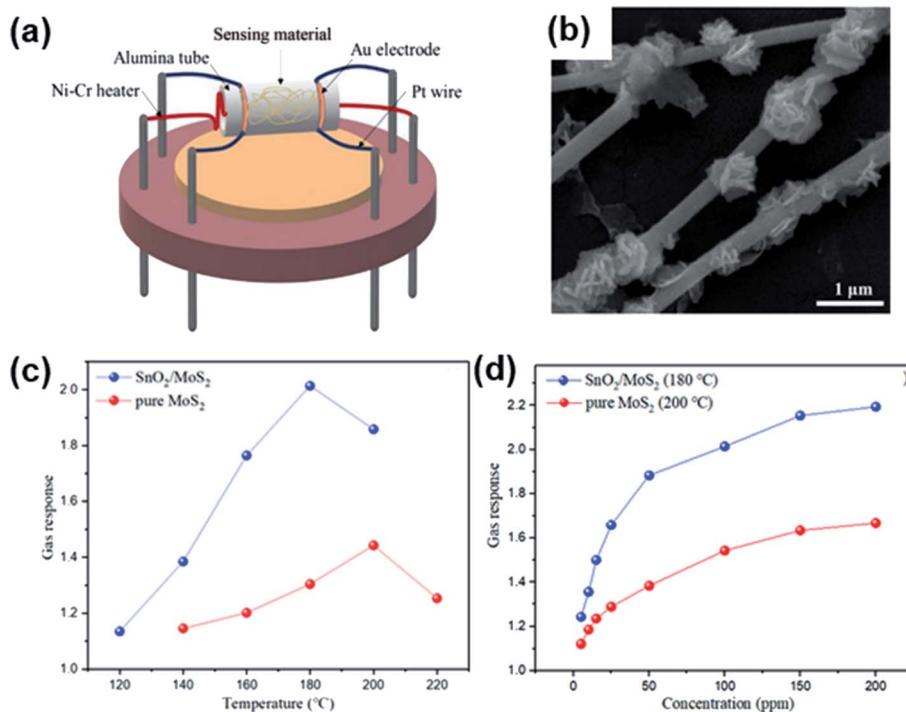
Fig. 20 (a) Schematic structure of a SnO$_2$/MoS$_2$ gas sensor. (b) SEM results of SnO$_2$/MoS$_2$ samples. (c) Gas response of sensor devices to 100 ppm CH$_4$ under different operating temperatures. (d) Gas response of two sensors to CH$_4$ with various concentrations. Reprinted with permission from ref. 163. Copyright 2019, Elsevier.

fabricated gas sensors based on rGO/MoS$_2$ hybrid films, which yielded flexible devices for formaldehyde detection at room temperature. The mechanisms for enhanced sensing performance of the rGO/MoS$_2$ hybrid films could be summarized as follows: in the hybrid film, MoS$_2$ nanosheets acted as the formaldehyde adsorbent and electron acceptor, mediating a two-stage electron transfer from formaldehyde and finally to rGO, which served as a conducting network and exhibited a p-type response. As shown in Fig. 21, Zhang *et al.* demonstrated some room temperature formaldehyde sensors based on a LBL self-assembled In$_2$O$_3$ nanocubes/flower-like MoS$_2$ nanofilm,[167] and Ni-doped In$_2$O$_3$/WS$_2$ nanocomposite.[168] They exhibited a low LOD of 15 ppb, good selectivity, repeatability, fast detection rate, and a fair logarithmic function toward formaldehyde concentration. The dramatically enhanced sensing performance of the Ni–In$_2$O$_3$/WS$_2$ sensor can be attributed to the Ni ion doping and synergistic interfacial incorporation of the In$_2$O$_3$/WS$_2$ heterojunction.

4.1.5 Ethanol. Volatile alcohols such as ethanol are often found in the chemical, medical, pharmaceutical, and food industries. They can induce nasal and mucous membrane inflammation, respiration disruption, eyesight disturbance, nerve disease, lung irritation, and even death after long-term exposure to even a low alcohol vapour concentration. On the other hand, because ethanol is a kind of flammable gas, it is essential to monitor its real-time concentration in workplaces. Moreover, ethanol is one of the typical biomarkers for lung cancer. Thus it requires developing a high-performance gas sensor for the detection of low concentration ethanol.

Many pristine metal sulfides, such as SnS NFKs,[34] CdS thin films,[171] hollow sphere CuS,[172] and β-In$_2$S$_3$ thin films,[173] were proposed for the detection of ethanol. At an OT of 300 °C, the CdS films show a high response% of 6300% and strong selectivity to alcohols in mixtures where aldehydes and other interferents are present. Their response and recovery time are speedy; however, their OTs are higher than 200 °C. Therefore, heterostructures of metal sulfides with metal oxides are introduced to enhance the sensing capability for alcohol detection. Both metal oxides and metal sulfide would have the same Fermi energy level at the interface, which results in a staggered band offset and a built-in internal electric field. When using the heterogeneous structure in a sensor, the electron generated from the adsorption reaction can easily move across the interface and transfer to the conductive band. In the context of metal sulfide/metal oxide heterostructures prepared through hydrothermal methods, MoS$_2$/SnO$_2$,[119] MoS$_2$/ZnO,[174] and MoS$_2$/TiO$_2$ (ref. 175) are three typical heterostructures. Among them, the MoS$_2$/SnO$_2$ sensor showed an ultra-high response% of 11 900% toward 200 ppm ethanol. All of them have fast response and recovery time (~20 s);; however, their OTs are higher than 150 °C. Thus a room-temperature ethanol sensor based on n-type α-Fe$_2$O$_3$ hollow microspheres on MoS$_2$ NSs prepared by the LBL self-assembly method was proposed and is shown in Fig. 22.[170] The α-Fe$_2$O$_3$/MoS$_2$ sensor has a low LOD of 1 ppm with high response, as well as a short response/recovery time of 6 s/5 s, which is shorter than those of α-Fe$_2$O$_3$ or MoS$_2$ devices. The enhancement performance of the α-Fe$_2$O$_3$/MoS$_2$ was attributed to the increased active sites for gas molecule

24958 | *J. Mater. Chem. A*, 2020, **8**, 24943–24976

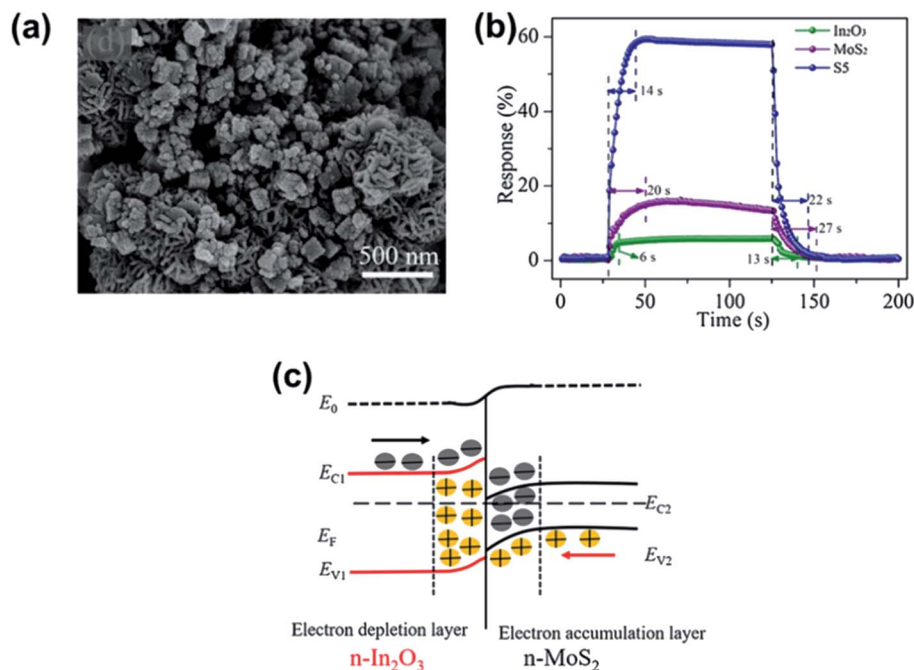This journal is © The Royal Society of Chemistry 2020

Fig. 21 (a) SEM images of In$_2$O$_3$ nanocubes/flower-like MoS$_2$ hybrids. (b) The response and recovery characteristics of In$_2$O$_3$, MoS$_2$ and In$_2$O$_3$/MoS$_2$ (S5) film sensors exposed to 50 ppm HCHO gas. (c) The energy band diagram for the n–n junction of the In$_2$O$_3$/MoS$_2$ film. Reprinted with permission from ref. 167. Copyright 2018, Elsevier.

adsorption, defects, or oxygen vacancies, when α-Fe$_2$O$_3$ into MoS$_2$ nanosheets. Besides, Li *et al.*[130] modified CdS NWs with CeO$_2$ NPs and found that the 5 wt% CeO$_2$/CdS n–n heterostructures exhibited a much higher response% toward 100 ppm ethanol (~5100%), which was 2.6 times larger than that of pure

CdS. The gas sensing properties of different metal sulfide-based ethanol sensors are listed in Table 5.

4.1.6 Liquefied petroleum gas (LPG). LPG is primarily composed of propane or butane and is widely used as fuels in vehicles, cooking, and heating appliances. LPG is potentially
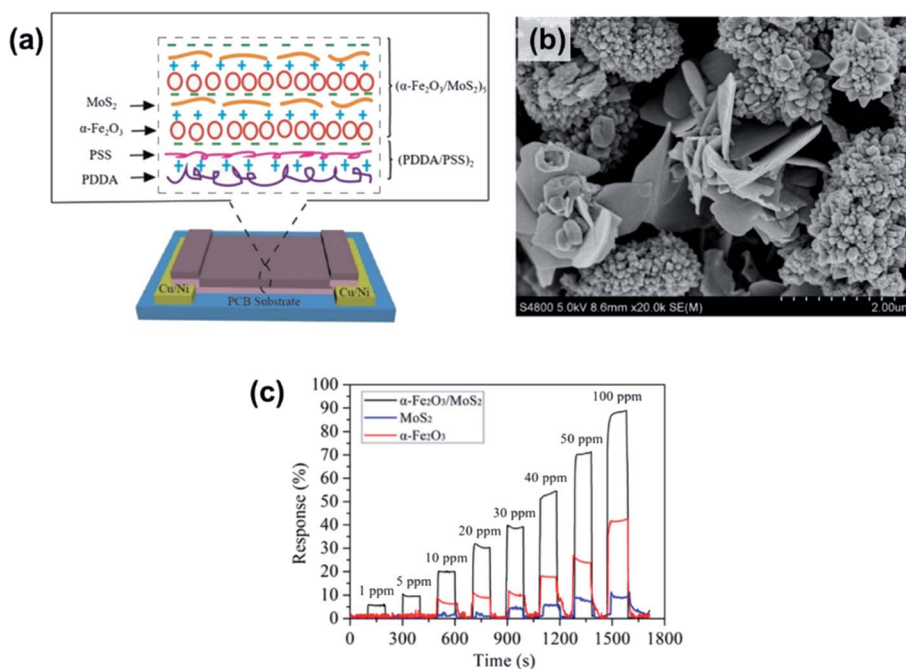
Fig. 22 (a) Schematic of an α-Fe$_2$O$_3$/MoS$_2$ gas sensor. (b) SEM image of the α-Fe$_2$O$_3$/MoS$_2$ nanocomposite. (c) Time-dependent response of the α-Fe$_2$O$_3$/MoS$_2$, α-Fe$_2$O$_3$, and MoS$_2$ film sensors towards various ethanol gas concentrations. Reprinted with permission from ref. 170. Copyright 2018, Elsevier.

This journal is © The Royal Society of Chemistry 2020

J. Mater. Chem. A, 2020, **8**, 24943–24976 | **24959**

Table 5 Gas sensing properties of metal sulfide-based sensors for ethanol

Material	Structure	Synthesis method	Concentration	Response (%)	LOD (ppm)	τ_s/τ_r	OT (°C)	Ref.
SnS	NFKs	Solid state reaction	10 ppm	130	—	2 s/9 s	200	34
CdS	Thin film	Screen printing	5 ppm	6300	—	~400 s/~400 s	300	171
CuS	Hollow spheres	Surfactant micelle-template inducing reaction	800 ppm	1300*	—	15 s/15 s	210	172
β-In_2S_3	Thin film	Spray pyrolysis	500 ppm	70*	—	150 s/155 s	350	173
MoS_2/SnO_2	Nanocomposites	Hydrothermal method	200 ppm	11 900*	—	~20 s/~20 s	280	119
MoS_2/ZnO	Nanocomposites	Hydrothermal method	50 ppm	4180*	—	~20 s/~20 s	260	174
0D-MoS_2/TiO_2	p–n heterojunction	Hydrothermal method	100 ppm	1320*	—	~20 s/~15 s	150	175
α-Fe_2O_3/MoS_2	Nanocomposite	LBL self-assembly	100 ppm	88.9	1	6 s/5 s	RT	170
CdS/CeO_2	NWs	Solvothermal method	100 ppm	5100*	—	12 s/3 s	161	130

dangerous because it may cause suffocation or even an explosion when it leaks accidentally. Various types of heterojunctions were found to achieve a high gas response due to their nm-level crystalline size and the specific surface area. Patil et al.[176] reported an LPG sensor based on p-polyaniline/n-PbS heterojunctions, which showed a maximum response up to 70% at 0.06 vol% LPG at room temperature. As shown in Fig. 23, Ladhe et al. successfully proposed an n-Bi_2S_3/p-PbS[177] heterojunction for room temperature LPG sensors, which showed ~70% response towards 1000 ppm LPG with fast response and recovery time. Moreover, n-Bi_2S_3/p-CuSCN,[178] n-CdO/p-PbS,[179] n-CdS/p-PbS,[180] CdS/SnO_2,[181] n-CdS/p-polyaniline,[182] and ZnS/polyacrylamide[183] demonstrated potential application in LPG detection. It is found that the alignment of energy bands at the interface of these heterojunctions shows the importance of gas sensing owing to the changes in barrier height of junction after exposure to the LPG gas environment.

4.2 Inorganic gases

Inorganic gases are essential for environment detection and as biomarkers in medical monitoring. The primary gases of interest are NH_3, NO, NO_2, CO_2, O_2, H_2S, SO_2, H_2, and humidity. This section will discuss metal sulfide-based devices for the detection of various inorganic gases.

4.2.1 NH_3. High concentrations of NH_3 could severely irritate the nose and throat of human beings and 1000 ppm vapours can cause pulmonary edema. Low concentrations of

NH_3 also could hurt the skin, eyes, and respiratory system after prolonged exposure.[184] Thus, the maximum permissible limit of NH_3 is 20 ppm for 8 hours.[7] Besides, NH_3 is present in the breath samples of healthy people and patients with renal disease. According to reports, the exhaled NH_3 concentration for healthy people ranges from 0.43 to 1.80 ppm, while that for end-stage renal disease patients ranges from 0.82 to 14.70 ppm.[185] Liu et al.[186] first presented high-performance room temperature chemical sensors based on Schottky-contact CVD MoS_2. The devices showed a response% of 20% toward 20 ppb of NO_2 and 40% toward 1 ppm of NH_3. The WS_2 NFK-based gas sensor showed p-type sensing behaviour and excellent response% of ~1500% towards 5 ppm NH_3 at room temperature.[187] Xiong et al.[188] fabricated an NH_3 sensor based on SnS_2 NFWs via a solvothermal process. The sensors exhibited a high response% of 640%, short response/recovery time of 40.6 s/624 s and a low LOD of 0.5 ppm NH_3. Late et al.[83] compared and analyzed the gas sensing behaviours of single-layer (SL) and multilayer (ML) MoS_2 transistor-based sensors towards NO_2, NH_3, and humidity, see Fig. 17. They found that the SL-MoS_2 sensor was unstable; the 5L-MoS_2 sensor showed a stronger response to a bias voltage, and the gas sensing response was enhanced after applying gate voltage. Moreover, phototransistor gas sensors of WS_2 (ref. 189) and ReS_2 (ref. 190) were employed for NH_3 gas detection, whose response and recovery times were fast.

Table 6 Gas sensing properties of metal sulfide-based sensors for LPG gases

Material	Synthesis method	Concentration (ppm)	Response (%)	LOD (ppm)	τ_s/τ_r	OT (°C)	Ref.
p-Polyaniline/n-PbS	Chemical bath deposition and electrodeposition	780	70	—	125 s/200 s	RT	176
n-Bi_2S_3/p-CuSCN	Chemical deposition	1370	70	—	180 s/142 s	RT	178
n-Bi_2S_3/p-PbS	Successive ionic layer adsorption and reaction (SILAR)	1000	72	—	300 s/170 s	RT	177
n-CdO/p-PbS	SILAR	1176	51.1	—	150 s/134 s	RT	179
n-CdS/p-PbS	SILAR	1200	60	—	120 s/105 s	RT	180
CdS/SnO_2	Screen printing	5000	7000	—	40 s/110 s	200	181
n-CdS/p-polyaniline	Electrodeposition	1040	80	—	105 s/165 s	RT	182
ZnS/polyacrylamide	Thermal frontal polymerization	5 vol%	62	—	180 s/480 s	RT	183
PbS/polyacrylamide			285	—	120 s/300 s		

24960 | J. Mater. Chem. A, 2020, **8**, 24943–24976

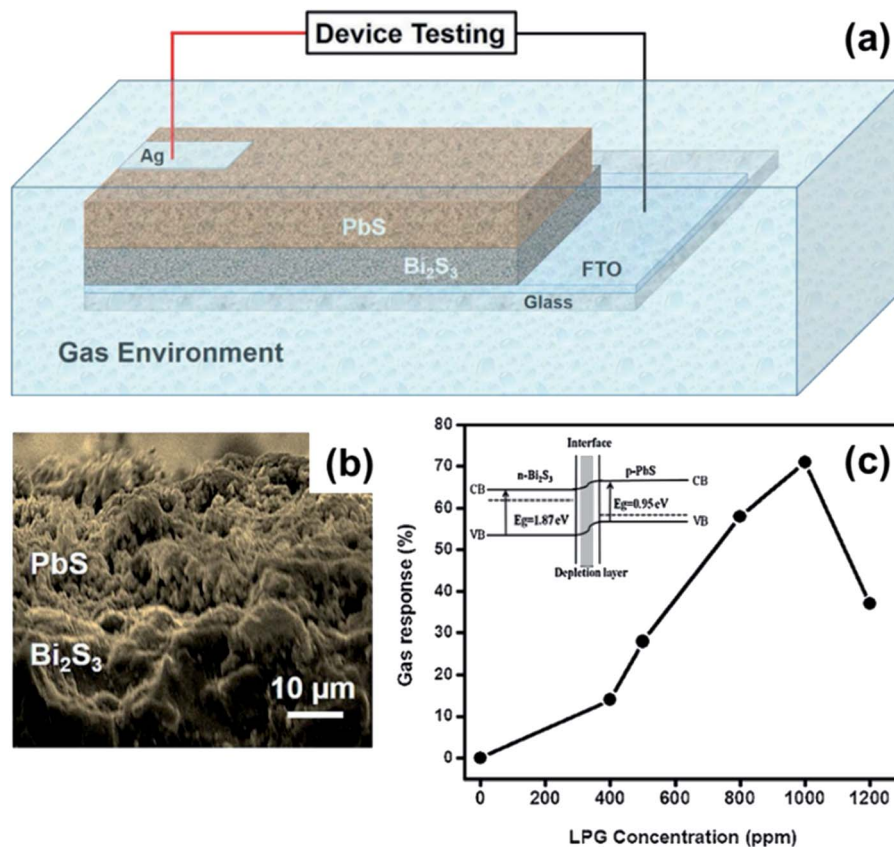This journal is © The Royal Society of Chemistry 2020

Fig. 23 (a) Schematic representation of the n-Bi_2S_3/p-PbS heterojunction device. (b) SEM image of the n-Bi_2S_3/p-PbS heterojunction. (c) The plot of variation in gas response (%) vs. LPG concentration (ppm) of the n-Bi_2S_3/p-PbS heterojunction. The inset shows the band diagram of the n-Bi_2S_3/p-PbS heterojunction. Reprinted with permission from ref. 177. Copyright 2017, Elsevier.

Benefitting from the interfacial Coulomb scattering and strong charge transfer, heterojunction-based devices have been used as NH_3 gas sensors. Zhang et al.[191] prepared MoS_2/ZnO nanocomposites comprising ZnO NRs and MoS_2 NSs, which could detect down to 12 ppb NH_3. Response/recovery times of 10 s/11 s were observed towards 50 ppm NH_3 at room temperature. The first MoS_2/Co_3O_4 nanocomposite NH_3 sensor was demonstrated by Sun et al., which showed a high response of 10.3% towards 100 ppb NH_3 with a response and recovery time of 98 s/100 s at room temperature, see Fig. 24a.[192] Moreover, an ultrahigh performance NH_3 sensor based on a nanoporous MoS_2/VS_2 heteroarchitecture was successfully fabricated. As shown in Fig. 24b, the gas-sensing performance investigated using a quartz crystal microbalance (QCM) reveals that MoS_2/
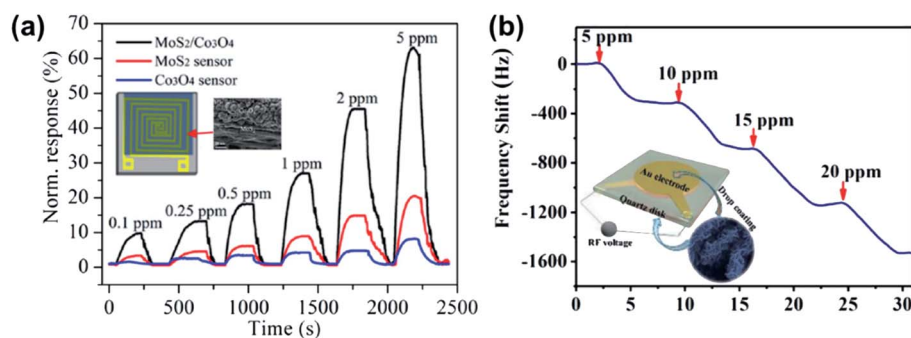
Fig. 24 (a) Normalized response of the MoS_2/Co_3O_4 MoS_2, and Co_3O_4 film sensors toward various NH_3 concentrations (inset: the schematic of the MoS_2/Co_3O_4 gas sensor and SEM image of MoS_2/Co_3O_4). Reprinted with permission from ref. 192. Copyright 2017, ACS Publishing. (b) The mass-normalized time-dependent frequency shifts of NH_3 adsorption on the MoS_2/VS_2 heterostructure at 40 °C (inset: illustration of the QCM experimental sensor prepared via drop-coating of the MoS_2/VS_2 heterostructure onto the Au electrode). Reprinted with permission from ref. 193. Copyright 2019, Wiley-VCH Verlag GmbH & Co. KGaA, Weinheim.

This journal is © The Royal Society of Chemistry 2020

J. Mater. Chem. A, 2020, 8, 24943–24976 | 24961

VS_2 exhibits a high adsorption uptake of $\Delta f = 344.5$ Hz toward 5 ppm NH_3, which is much better than that of previously reported QCM NH_3 sensors.[193] Other p–n heterojunction gas sensors, for instance, 2D WS_2 NSs decorated with TiO_2 QDs, were proved to have a high response to NH_3 gas at room temperature.[194] Xu et al.[117] and Leonardi et al.[195] synthesized SnO_2–SnS_2 p–n heterojunctions by the oxidation of SnS_2 at high annealing temperature. The devices exhibited fast response time (11 s) at room temperature, much faster than that of other NH_3 sensors. For other heterojunction gas sensors, Pr-SnS_2/ZnS,[129] PbS/TiO_2,[196] and PbS/NaS_2 (ref. 197) were proposed as sensing materials for NH_3 detection. Pr-SnS_2/ZnS showed a high response% of 1303% and fast response/recovery time of 6 s/13 s towards 50 ppm NH_3 at an OT of 160 °C, and PbS/NaS_2 had a high response% of 30 000% when exposed to 8.08% NH_3 at room temperature. The gas-sensing performances of various metal sulfide-based NH_3 gas sensors are listed in Table 7. It was found that the sensor based on metal oxide/metal sulfide heterojunctions exhibits higher response% and lower LOD.

4.2.2 NO_2 and NO. NO_2 is one of the most abundant air pollutants and is primarily emitted by fossil fuel burning, road traffic, indoor combustion,[201] and biomass burning.[202] It induces acid rain and photochemical smog. High concentrations of NO_2 can irritate the human respiratory system. Long exposures to low NO_2 concentrations also cause the development of asthma and respiratory symptoms. NO in exhaled breath is associated with inflammation of the air path, such as asthma and bronchiectasis. It is a typical biomarker for chronic obstructive pulmonary disease and nasal polyposis.[203] The recommended concentration of NO for healthy people is below 25 ppb; when it is higher than 50 ppb, it is perhaps a sign of airway inflammation.[204] Notably, NO is easily oxidized to NO_2, indicating that it is challenging to detect NO directly using semiconductor gas sensors. Sometimes, the concentration of NO is usually reflected indirectly by detecting NO_2. Li et al.[82] proposed a MoS_2 FET NO sensor and compared and analyzed the sensors with monolayer, bilayer, trilayer, and quadrilayer MoS_2. The response of the monolayer sensor is rapid and dramatic but unstable. In contrast, the multilayer sensors are stable and show sensitive responses down to a LOD of 0.8 ppm NO. TaS_2 NSs exfoliated by electrochemical lithium intercalation have been employed for the detection of NO and showed a high response% of 6000% towards 500 ppm NO and exhibited a sub-ppm LOD.[60] A TaS_3 nanofibre NO gas sensor exhibited a high sensitivity of 4.48° μM^{-1} and a low LOD of 0.48 ppb, well under the allowed value set by the WHO, see Fig. 25.[65] The different types of NO and NO_2 gas sensors based on metal sulfides are summarised in Table 8.

Wang et al.[33] proposed a NO_2 gas sensor using large-sized SnS thin crystals, which present a high response% of 20% towards NO_2 at a 100 ppb concentration, as well as superior selectivity, low LOD (≪100 ppb), and reversibility at room temperature. Benefitting from a large excitation Bohr radius (18 nm), PbS thin films were synthesized and applied in NO_2 detection, and they exhibited a response% of 35% for 50 ppm NO_2 at 150 °C with a rapid response time of 6 s.[207] Recently, Sonker et al.[205] used a sol–gel method for fabricating CdS NPs, which can detect 20 ppm NO_2 gas with a response% of 17 300%

Table 7 Literature study on the gas-sensing performance of metal sulfide-based NH_3 gas sensors

Material	Structure	Synthesis method	Concentration	Response (%)	LOD (ppm)	τ_s/τ_r	OT (°C)	Ref.
MoS_2 (green illumination)	Transistor	ME	1000 ppm	86	—	~800 s/1500 s	RT	83
WS_2	NFKs	Ball milling	5 ppm	~1400*	—	~120 s/~150 s	RT	187
	Phototransistor	ME	—	—	—	2.6 s/56 s	RT	189
ReS_2	Phototransistor	ME	—	—	—	~70 ms/~70 ms	RT	190
SnS_2	2D SnS_2 with sulfur vacancies	Chemical exfoliation	500 ppm	420	—	16 s/450 s	RT	109
	NFWs	Solvothermal method	100 ppm	640*	0.5	40.6 s/624 s	200	188
	NFWs	Hydrothermal method	5 ppm	21.6	—	40–50 s/100–120 s	RT	198
Graphene/MoS_2	Heterostructure	ME-MoS_2 CVD-graphene	100 ppm	6	—	NA/30 min	150	199
MoS_2/ZnO	Nanocomposites	LBL self-assembly	50 ppm	46.2	0.012	10 s/11 s	RT	191
MoS_2/CuO	Nanoworms	Sputtering	100 ppm	47	5	17 s/26 s	RT	200
MoS_2/Co_3O_4	Nanocomposites	LBL self-assembly	0.1 ppm	10.3	0.1	98 s/100 s	RT	192
MoS_2/VS_2	Heterostructure, QCM	Hydrothermal method	5 ppm	$\Delta f = 344.5$ Hz	—	—	40	193
WS_2/TiO_2	Nanocomposites	Mixture solution	500 ppm	56.69	20	200 s/174.43 ± 13.75 s	RT	194
SnS_2/SnO_2	NFKs	Annealing	50 ppm	40*	—	~60 s/~300 s	130	195
	Hybrids	Oxidation	10 ppm	16*	—	11 s/NA	RT	117
Pr-SnS_2/ZnS	NFWs	Hydrothermal method	50 ppm	1303*	—	6 s/13 s	160	129
PbS QDs/TiO_2	NTs	SILAR	100 ppm	1649*	2	~10 s/~10 s	RT	196
PbS/NaS_2	NPs	—	8.08%	30 000*	—	46 s/67 s	RT	197

24962 | J. Mater. Chem. A, 2020, **8**, 24943–24976

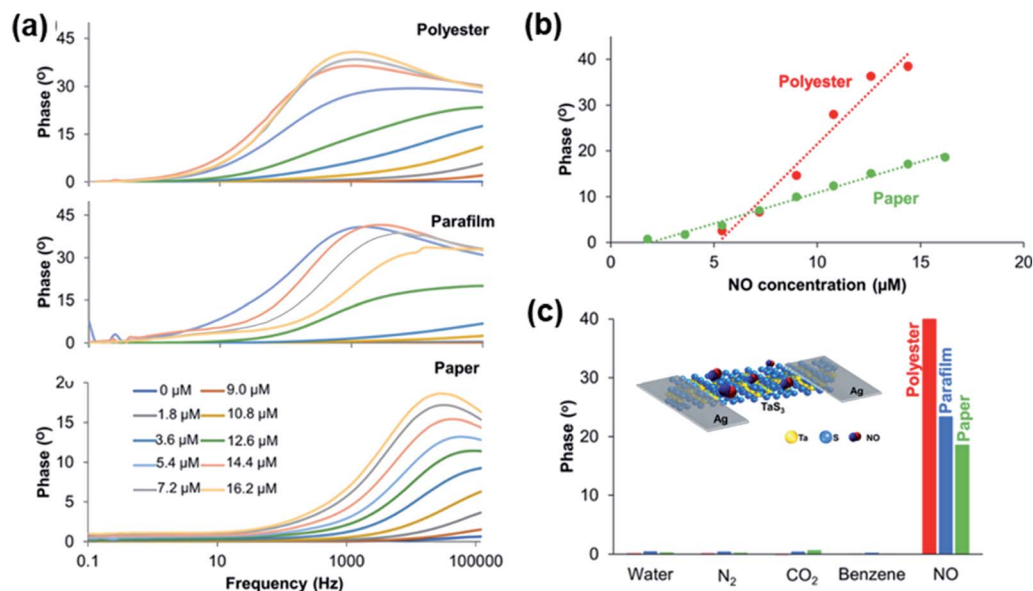This journal is © The Royal Society of Chemistry 2020

Fig. 25 (a) Impedance responses of the TaS$_3$ sensor fabricated in polyester, parafilm, and paper under different NO concentrations from 0 to 16.2 μM. (b) Calibration curves of the TaS$_3$ gas sensor fabricated in polyester and paper at different NO concentrations. (c) Selectivity study comparison of the TaS$_3$ gas sensor fabricated in all configurations (paper, parafilm, and polyester). The inset image shows the schematic representation of various TaS$_3$ nanofiber-based devices. Reprinted with permission from ref. 65. Copyright 2018, ACS Publishing.

at 70 °C. Donarelli et al.[29] found that LPE-MoS$_2$ NFKs after annealing in air at 150 °C and 250 °C can show a p-type and n-type conductivity, respectively. The p-type MoS$_2$ showed 15% response towards 1 ppm with fast response/recovery time (11 s/ 22 s), while the n-type MoS$_2$ exhibited a higher response% of 480% and a lower LOD of 20 ppb. Xu et al.[208] synthesized ultra-thin WS$_2$ NSs through a hydrothermal and calcination process, which showed a high response of 9.3% after exposure to 0.1 ppm NO$_2$ gas at room temperature. Ko et al.[211] proved that the WS$_2$ gas sensor showed dramatically improved response (667%) and recovery upon NO$_2$ exposure after functionalization with AgNWs. Another WS$_2$/WO$_3$-based gas sensor showed an excellent LOD of 40 ppb in dry air for NO$_2$ at an OT of 150 °C.[215] 2D SnS$_2$-based gas sensors presented a high response% of 3533% toward 10 ppm NO$_2$ and showed highly selective and reversible NO$_2$ sensing.[210] Kim et al.[59] fabricated a room temperature NO$_2$ sensor using 2D NbS$_2$, which showed a response% of 2832% toward 10 ppm NO$_2$ and a low LOD of 241.02 ppb.

For metal–metal sulfide Schottky junctions, Liu et al.[186] observed a considerable SB in the Ti/Au electrodes and at the CVD-MoS$_2$ contact interface, which showed a conductance change of 2–3 orders of magnitude upon exposure to sub-ppb level concentrations of NO$_2$ and NH$_3$. Besides, vdW vertical Schottky junctions of graphene and semiconductors have attracted considerable attention as emerging transducers for gas sensors. Tabata et al.[212] deeply analyzed the NO$_2$ gas-sensing performance of a graphene/MoS$_2$-based gas sensor, where the SBH was modulated by bias- and gate-voltage. The device exhibited an ultra-high response% of 160 000% after 10 min exposure to NO$_2$. To know the difference between the Schottky junction of metal–metal sulfides and graphene–metal sulfides,

Pham et al.[114] compared and analyzed the gas-sensing performances of CVD MoS$_2$ with Au metal electrodes (Au–MoS$_2$–Au), graphene electrodes (Gr–MoS$_2$–Gr), and graphene/Au electrodes (Au/Gr–MoS$_2$–Gr/Au). The resulting Au/Gr–MoS$_2$–Gr/Au gas sensor under red light illumination showed a significant enhancement of the device response% toward 150 ppb of NO$_2$ gas reaching 500% (see Fig. 26). The excellent performance could be attributed to the encapsulation of graphene electrodes with the Au layer affecting the work function of graphene, resulting in an increasing SBH. Furthermore, Au/Gr electrodes could hinder the negative effects of the modulation of the work function induced by the doped graphene with NO$_2$ molecules.

For heterojunction-based devices, MoS$_2$/SnO$_2$ p–n heterojunctions were constructed and used for ethanol, TMA, and NO$_2$ gas sensing.[119-121] They exhibited high sensitivity, lower OT, excellent sensing selectivity, and outstanding long-term stability. Shao et al.[214] fabricated rGO–MoS$_2$–CdS nanocomposite films via solvothermal treatment and analyzed the sensing performance. The results showed a largely enhanced sensor response of 27.4% toward 0.2 ppm NO$_2$, approximately 7 times higher than the value for the rGO–MoS$_2$ based gas sensor. Moreover, a SnO$_2$–SnS$_2$ p–n heterojunction was employed in the NO$_2$ gas sensor.[117,148]

A FET gas sensor was used for NO$_2$ gas sensing because the conductance of the channel can be modulated by applying different bias voltages on the gate electrode. Late et al.[83] analyzed the NO$_2$ sensing behaviours of the MoS$_2$ transistor, Fig. 17. The response was enhanced after applying gate bias. Similarly, WS$_2$ (ref. 189) and ReS$_2$ (ref. 190) FETs were employed to detect different gases, such as O$_2$, NH$_3$, and NO$_2$. As mentioned in Section 3.5, the strong electron transfer between the FET channel materials and the gas molecule could alter the

This journal is © The Royal Society of Chemistry 2020

J. Mater. Chem. A, 2020, 8, 24943–24976 | 24963

carrier concentration of the channel, modulate the mobility, further affect semiconductor work function, and finally change the current of the FET.[221,222] Based on this mechanism, our group analyzed a WS$_2$/IGZO p–n junction-based gas sensor in chemiresistor and transistor mode, respectively.[217] It was found that the transistor shows an ultra-high response after exposure to NO$_2$, with a response% of 499 400% for 300 ppm, which is ~27 times higher than that in chemiresistor mode (see Fig. 27a–c). One special case reported by Tabata et al.[212] is the graphene/MoS$_2$ heterojunction (GMH) sensor. As shown in Fig. 27d–f, the device had a high response% to NO$_2$ of 160 000% at a 0 V back-gate voltage (V_{BG}); however, when V_{BG} = 40 V, the response% decreased to 600%. They found that the drain current was primarily determined by the SBH at the counter Schottky diode of the MoS$_2$/Ti contact, and the NO$_2$-induced modulation in the SBH at the GMH was not reflected in the sensor response. Last but not least, the SAW NO$_2$ sensor uses SnS CQDs as the sensing layer and is fabricated on a quartz substrate.[140] The sensor could detect a low concentration of NO$_2$ gas at room temperature with a good efficiency and selectivity (see Fig. 19).

4.2.3 CO$_2$ and O$_2$. CO$_2$ is the fourth most abundant component of dry air. Tests have shown that 5% CO$_2$ is not harmful to humans if sufficient oxygen is present, but once the O$_2$ concentration is less than 17%, even 4% CO$_2$ can cause severe poisoning. Considering that the ambient concentration of CO$_2$ is approximately 0.03%, the required LOD for CO$_2$

Table 8 Literature study on the NO$_x$ sensing performance of metal sulfide-based devices

Material	Structure	Synthesis method	Analyte	Concentration (ppm)	Response (%)	LOD	τ_s/τ_r	OT (°C)	Ref.
SnS	Thin crystal	Solvothermal method	NO$_2$	0.1	20	—	NA/5 s	RT	33
CdS	Thin film	Chemical route	NO$_2$	20	17 300	—	331 s/207 s	70	205
	Thin film	Chemical bath deposition	NO$_2$	200	61	—	50 s/NA	RT	206
PbS	Thin film	Chemical bath deposition	NO$_2$	100	74	—	20 s/36 s	38	100
	Thin film	SILAR	NO$_2$	50	35	—	6 s/97 s	150	207
TaS$_2$	NSs	Electrochemical lithium-intercalation	NO	5	60	—	—	RT	60
TaS$_3$	Nanofibres	Vapour-phase growth	NO	—	Sensitivity 4.48° µM^{-1}	0.48 ppb	—	RT	65
MoS$_2$	Transistor	ME	NO	2	80	0.8 ppm	—	RT	82
	Transistor	ME	NO$_2$	1000	1372	—	~800 s/1500 s	RT (green light)	83
	NFKs	LPE	NO$_2$	1	15 (p-type) 480 (n-type)	20 ppb	11 s/22 s 41 s/39 s	200	29
WS$_2$	NSs	Hydrothermal method & calcination	NO$_2$	0.1	9.3	100 ppb	5 min/25 min	RT	208
SnS$_2$	2D	Ball milling	NO$_2$	10	2000	—	6/40 s	250	209
	2D flakes	Solvothermal method	NO$_2$	10	3533*	—	~170 s/~140 s	120	210
NbS$_2$	NSs	CVD	NO$_2$	10	2832	241.02 ppb	3000 s/9000 s	RT	59
Ag NWs–WS$_2$	NSs	ALD	NO$_2$	500	667	—	5 min/10 min	RT	211
Al/MoS$_2$	Schottky contact	CVD	NO$_2$	10	60	—	~5 min/~20 min	RT	111
Au/Gr–MoS$_2$–Gr/Au	Schottky contact	CVD	NO$_2$	0.15	500*	0.1 ppb	~1000 s/~700 s	RT (red light)	114
Gr–MoS$_2$	Schottky contact	ME	NO$_2$	1	160 000	—	—	RT	212
MoS$_2$/SnO$_2$	Heterostructures	Chemical methods	NO$_2$	5	1770*	—	74 s/NA	RT	121
MoS$_2$/ZnO	NWs	Hydrothermal method & CVD	NO$_2$	50	31.2	0.2 ppm	60 min/65 min	200	213
rGO–MoS$_2$–CdS	Nanocomposite	Hydrothermal method	NO$_2$	0.2	27.4	—	25 s/34 s	75	214
WS$_2$/WO$_3$	Nanocomposites	Oxidation	NO$_2$	0.4	100*	400 ppb	—	150	215
WS$_2$/ZnS	Heterostructures	LPE-WS$_2$, chemical method	NO$_2$	5	3150*	10 ppb	4 s/~400 s	RT	216
WS$_2$/IGZO	Heterojunction	CVD, sputtering	NO$_2$	5 300	6820 499 400	26 ppb	—	RT	217
SnS$_2$/SnO$_2$	Nanocomposites	Oxidation	NO$_2$	8	430*	1 ppm	159 s/297 s	80	148
SnS$_2$/SiO$_2$	Nanograins	CVD	NO$_2$	10	701	408.9 ppb	272.8 s/3800.4 s	RT	218
SnS$_2$/rGO	Heterojunction	Hydrothermal method	NO$_2$	8	49.8	8.7 ppb	NA/76 s	RT	219
PbS QDs/MoS$_2$	Nanocomposites	Hydrothermal method & chemical precipitation	NO$_2$	100	~23	—	30 s/235 s	RT	220
ZnS/CuO	NWs	Thermal evaporation & solvothermal method	NO$_2$	5	955*	—	45 s/170 s	RT (UV light)	133

24964 | J. Mater. Chem. A, 2020, **8**, 24943–24976
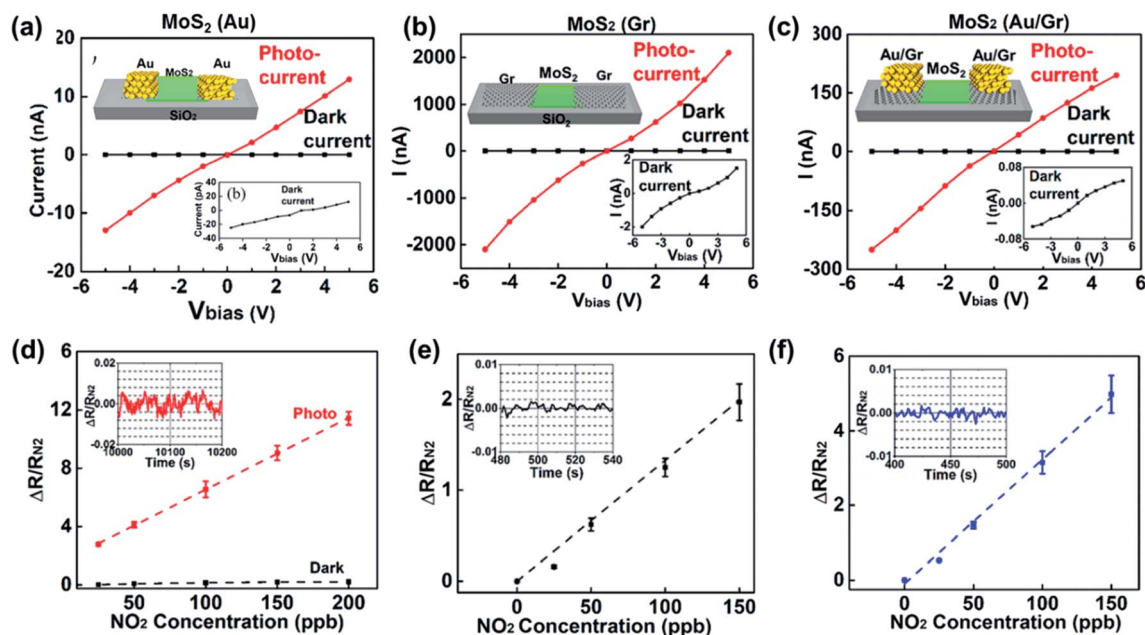
This journal is © The Royal Society of Chemistry 2020

Fig. 26 $I-V$ curves under red LED illumination (red line) and in the dark (black line) of (a) Au–MoS$_2$–Au, (b) Gr–MoS$_2$–Gr, and (c) Au/Gr–MoS$_2$–Gr/Au devices. The insets show the corresponding schematics of the devices and expanded $I-V$ curves in the dark. (d–f) Dependence of the normalized amplitude of the resistance change of (d) Au–MoS$_2$–Au, (e) Gr–MoS$_2$–Gr, and (f) Au/Gr–MoS$_2$–Gr/Au devices on the concentration of NO$_2$ gas. The inset image shows a temporal trace of the experimentally recorded noise of $\Delta R/R_{N_2}$. All data were collected under a dc bias of 5 V. Reprinted with permission from ref. 114. Copyright 2019, ACS Publishing.

sensors could be at the ppm-level. Because CO$_2$ is a kind of nonpolar gas owing to its linear and symmetrical structure, the adsorption energy between CO$_2$ and the surface of metal sulfides is low. To this end, a new optical CO$_2$ sensor based on the colorimetric change of the pH indicator α-naphtholph-thalein with the internal reference fluorescent CIS/ZnS QDs was developed.[223,224] The experimental result reveals that the new optical CO$_2$ sensor has a response% of $(I_{100} - I_0)/I_0 \times 100\% = 1240\%$. Similarly, Chu *et al.*[225] developed a CdSe/ZnS QD based

optical fibre CO$_2$ sensor, which showed a high response% of $(R_0 - R)/R \times 100\% = 84\%$ and exhibited a uniquely linear response to CO$_2$ concentrations in the range of 0–100%. The gas testing setup of the fibre-optic CO$_2$ sensor is shown in Fig. 28, and this testing method can quantitively measure the CO$_2$ concentration; however, it cannot detect changes of the fluorescence spectra in real-time.

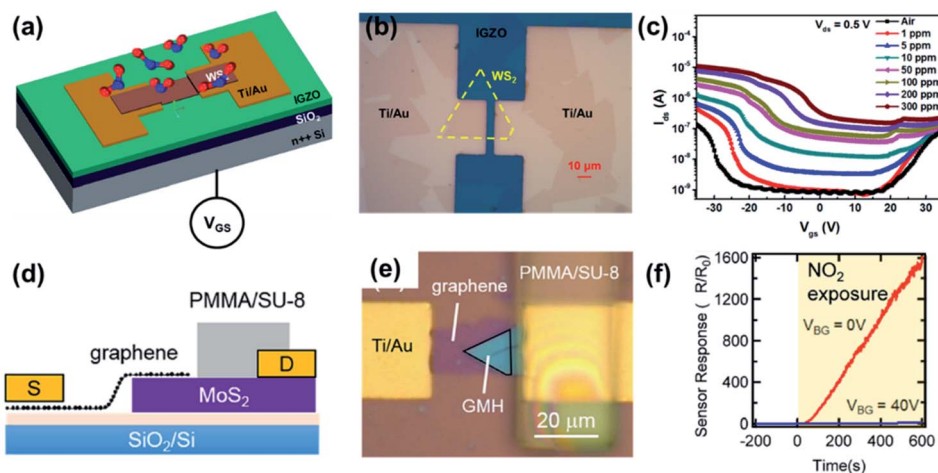O$_2$ is a major component of air and greatly affects metal corrosion protection, fuel combustion, and food storage. It is

Fig. 27 (a) Schematic diagram and (b) optical image of the WS$_2$/IGZO transistor. (c) Transfer curves of the WS$_2$/IGZO transistor under different NO$_2$ concentrations. Reprinted with permission from ref. 217. Copyright 2019, ACS Publishing. (d) Schematic diagram and (e) optical image of the graphene/MoS$_2$ heterojunction (GMH) device with a gas barrier layer. (f) Time-dependent sensor responses of GMH under different gate voltages (V_{BG} = 0 and 40 V). Reprinted with permission from ref. 212. Copyright 2019, ACS Publishing.
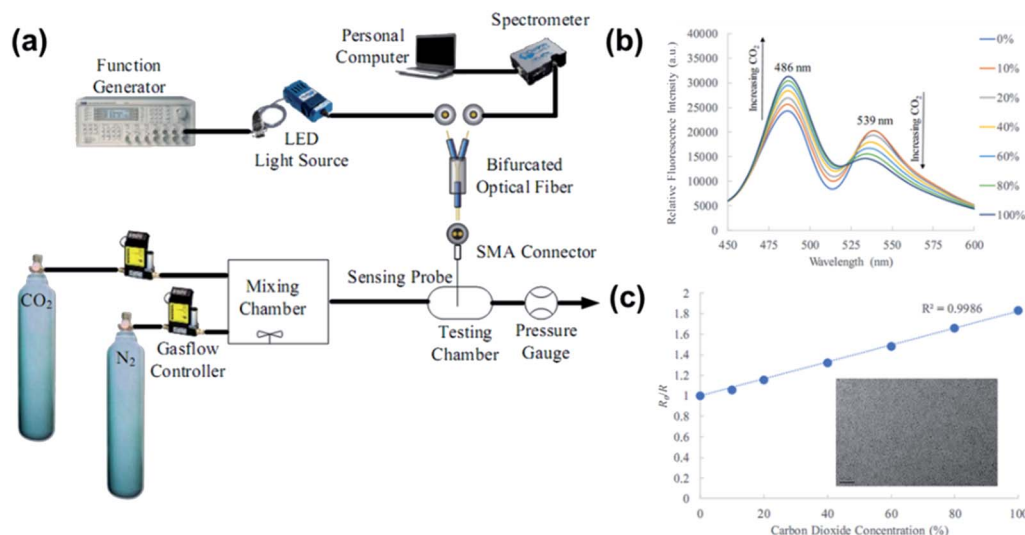
This journal is © The Royal Society of Chemistry 2020

J. Mater. Chem. A, 2020, **8**, 24943–24976 | **24965**

Fig. 28 (a) Experimental setup for the ratiometric optical fibre CO_2 sensing. (b) Fluorescence spectra of the ratiometric optical fibre sensor under different CO_2 concentrations. (c) Calibration curve of the ratiometric optical fibre CO_2 sensor at 0–100% concentration. Reprinted with permission from ref. 225. Copyright 2019, SPIE publishing.

essential to monitor the O_2 content in industrial production and medical care. Metal sulfide nanomaterials for O_2 sensing have not been extensively studied. Kim et al.[226] prepared MoS_2 NP-based gas sensors through LPE methods and investigated their O_2 sensing behaviour, which showed a high response% of 769% towards a 2% concentration of O_2 and a low LOD at the ppb level. Li et al.[227] proposed a 2D SnS_2-based sensor, which provided high and reversible responses to O_2 pulses in the range of 0 to 20% volume in the dark at 150 °C. They applied UV irradiation for improving the O_2 sensing performance. Karami et al.[228] synthesized SnS–SnO_2 nanocomposites and used them as O_2 gas-sensing agents, which showed a high dynamic range, high sensitivity to O_2, fast response time, and low memory effect without any interference from the other gases (OT = 128 °C).

4.2.4 H_2S and SO_2. Both H_2S and SO_2 are hazardous gases and atmospheric pollutants. H_2S smells like rotten eggs and irritates people's eyes, nose, and throat. Long-term exposure to H_2S above 100 ppm can cause death. In the human body, H_2S is

a kind of metabolic product that has an unpleasant odor and is associated with halitosis. SO_2 is highly corrosive and easily oxidized to create sulfuric acid in the air. These two gases pose significant threats to the environment and human health and require accurate measurement.

PbS CQDs have been used as H_2S gas sensing materials, and they exhibit a response% of 421 700% towards 50 ppm H_2S, which is considerably high, and a fast response/recovery time of 23 s/171 s.[101] Metal oxide/metal sulfide heterojunctions, such as ZnS/ZnO[132] and CuS/CuO,[229] have been employed for the detection of H_2S gas, see Fig. 29. Souda and Shimizu[106] tested various metal monosulfide-based gas sensors (NiS, CdS, SnS, and PbS), which showed a high SO_2 response at 300–400 °C. The CdS-based sensor has the best sensing performance, whose response was almost linear with the logarithm of SO_2 concentration between 20 and 200 ppm. It has a 90% response% to 100 ppm SO_2 but the response time is as long as 2–4 min and it works at 400 °C. Zhang et al.[90] fabricated a room-temperature
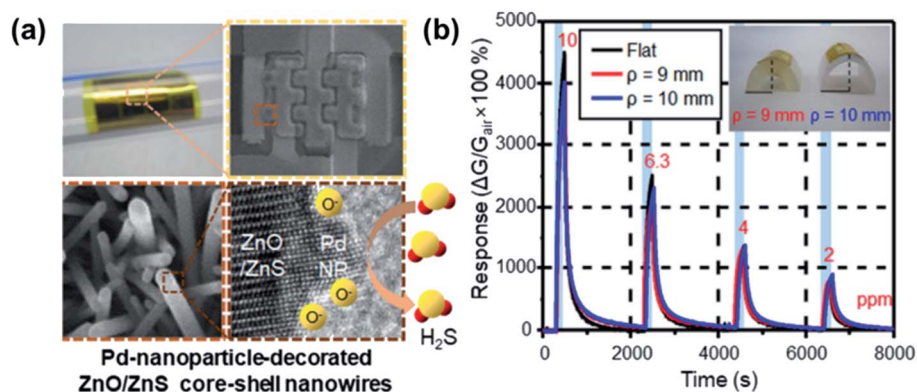

Fig. 29 (a) Photograph and SEM and TEM images of a ZnO/ZnS NW sensor on a flexible substrate and (b) the H_2S gas sensing result. Reprinted with permission from ref. 132. Copyright 2019, ACS Publishing.

24966 | J. Mater. Chem. A, 2020, **8**, 24943–24976

This journal is © The Royal Society of Chemistry 2020

SO_2 sensor using metal-doped MoS_2 NFWs. The Ni-doped MoS_2 showed the best performance among different metal-doped MoS_2 (*i.e.*, Ni-, Fe-, Co-doped MoS_2) compounds and showed a 7.4% response% toward 5 ppm SO_2 and a low LOD of 250 ppb. Table 9 summarises the gas sensing properties of metal sulfide-based sensors for CO_2, O_2, H_2S, and SO_2. It is clear that PbS is an ideal candidate for H_2S gas detection, and there is room for functionalized MoS_2 for the detection of other types of gases (*i.e.*, SO_2 and O_2).

4.2.5 H_2. H_2 is a colorless, tasteless, odorless, and flammable gas. It is an excellent candidate carrier in the clean energy area, such as for automobile engines and fuel cells. Thus it requires high-performance H_2 sensors in mobile transportation as well as household environments. Hafeez *et al.*[231] compared and analyzed the H_2 gas-sensing performance of ZnS nanostructures with different morphologies (NWs, nanodots

(NDs), and nanoleaves (NLs)). They found that NWs have higher cohesive energy than others, which showed a response% of 800% towards 50 000 ppm H_2 gas at an OT of 230 °C. Sabah *et al.*[104] prepared a CuS thin film by spray pyrolysis deposition using deionized water and used it for the detection of H_2 gases. Linganiso *et al.*[105] synthesized NiS nanostructures and measured the H_2 gas sensitivity, which has 158% response to 100 ppm H_2 at 300 °C. Baek and Kim[107] fabricated an H_2 sensor with few-layered Pd-doped MoS_2, which exhibited a 35.3% response% when exposed to a 1% H_2-containing gas. In contrast, the pristine MoS_2 showed no reaction. Perrozzi *et al.*[215] demonstrated that the H_2 gas sensor based on WS_2/WO_3 hierarchical heterostructures with surface oxygen and sulfur vacancies had a high response% of 430% towards 500 ppm H_2 and exhibited a low LOD of 1 ppm. The sensors showed no substantial humidity cross-sensitivity effects, indicating the

Table 9 Gas sensing properties of metal sulfide-based sensors for inorganic gases

Material	Structure	Synthesis method	Analyte	Concentration	Response (%)	LOD	τ_s/τ_r	OT (°C)	Ref.
CIS/ZnS (optical)	QDs	Hydrothermal method	CO_2	100 vol%	1240*	—	—	RT	223
	QDs	Hydrothermal method		100 vol%	99.6	—	—	RT	224
CdSe/ZnS (optical)	QDs	Hydrothermal method	CO_2	100 vol%	84*	—	—	RT	225
MoS_2	NPs	Chemical exfoliation	O_2	2 vol%	769*	49.96 ppb	—	300	226
GaS	NSs	ME	O_2	—	—	—	—	—	230
SnS_2	2D flakes	Wet-chemical method	O_2	2 vol%	160*	—	10 min/15 min	130 (UV)	227
$SnS–SnO_2$	Nanocomposite	Electrochemical deposition	O_2	19 ppm	21 000	900 ppb	52 s/38 s	128	228
PbS	QDs	Deposition	H_2S	500 ppm	421 700*	—	23 s/171 s	135	101
CuS/CuO	Nanocomposite	Solvothermal method	H_2S	1.88%	313 900	—	75 s/67 s	RT	229
ZnS/ZnO	Nanocomposite	Hydrothermal method	H_2S	10 ppm	4491	—	99 s/88 s	95	132
CdS	2D flakes	Wet-chemical method	SO_2	100 ppm	—	—	15 min/NA	400	106
Ni-doped MoS_2	NFWs	Hydrothermal method	SO_2	5 ppm	7.4	250 ppb	51 s/73 s	RT	90

Table 10 Gas sensing properties of metal sulfide-based sensors for H_2

| Material	Structure	Synthesis method	Concentration	Response (%)	LOD (ppm)	τ_s/τ_r	OT (°C)	Ref.
ZnS	Nanostructures	PVD	50 000 ppm	800	—	—	230	231
CuS	Film	Spray pyrolysis	1000 ppm	9890	—	16/34 s	RT	104
Au-coated NiS	Nanostructures	Hydrothermal method	95%	58*	—	~50 s/~100 s	300	105
Pd-doped MoS_2	NSs	Solution processing	1%	35.3	50	~500 s/~1200 s	RT	107
WS_2/WO_3	Nanocomposites	Oxidation	500 ppm	430*	1	—	150	215
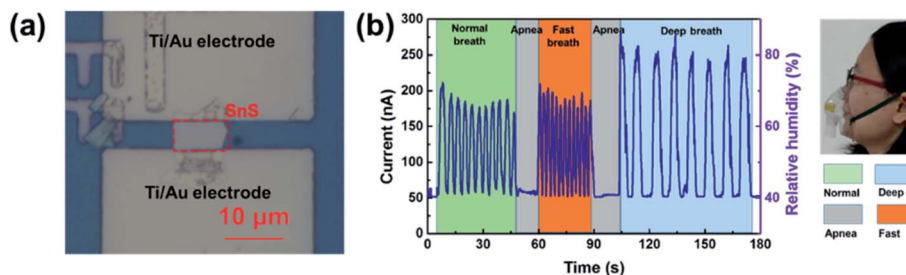
Fig. 30 (a) Optical image of a SnS nanoflake-based sensor. (b) Real-time respiration detection by using a SnS humidity sensor. Reprinted with permission from ref. 71. Copyright 2019, © IOP Publishing. All rights reserved.

This journal is © The Royal Society of Chemistry 2020

J. Mater. Chem. A, 2020, **8**, 24943–24976 | **24967**

Table 11 The humidity sensing performances of fibre-optic sensing devices in the literature

Device structure	τ_s (s)	τ_r (s)	Dynamic range of response	Ref.
MoS$_2$-coated ESMF	0.066	2.395	0.487 dB/(20–80% RH)	237
MoS$_2$-coated SPF	0.85	0.85	13.5 dB/(40–85% RH)	138
WS$_2$-coated SPF	1	4	9 dB/(37–90% RH)	236

great potential application in real-world H$_2$ detection. Various metal sulfide-based H$_2$ gas sensors are listed in Table 10.

4.2.6 Humidity sensor. Humidity sensors have been successfully used in various fields, such as environmental monitoring, industrial production, and the medical instrumentation field. Tang et al.[71] demonstrated that SnS NFKs could be used for real-time respiration detection due to their high response% of 2 491 000% and fast response/recovery time (6 s/4 s), suitable for health monitoring, see Fig. 30. Guo et al. fabricated transparent and flexible WS$_2$ based humidity sensors for electronic skin, with a wide relative humidity range (up to 90%) with fast response and recovery in a few seconds.[232] Feng et al.[233] fabricated a flexible touchless positioning interface based on a highly sensitive VS$_2$ NS humidity sensor. However, VS$_2$ ultra-thin NSs have poor stability. To improve the stability, Chen et al. proposed a MoS$_2$/VS$_2$ (ref. 35) sensor; after 30 days its response% was maintained at around 579 750%, indicating that the nanocomposite sensor has good long-term stability. Chemiresistor sensors based on ReS$_2$ NSs[234] and MoS$_2$ decorated with Pt NPs[235] were reported. The Pt–MoS$_2$ sensor showed

a high and stable response% of 400 000% at 85% RH when tested over a few months.

Apart from the chemiresistor sensor, the optical, impedance, and capacitive sensors were employed for the detection of humidity. Luo et al.[236] and Li et al.[138] demonstrated all-fibre-optic humidity sensors comprising a WS$_2$ and MoS$_2$ film overlay on an SPF, respectively. They used a 1550 nm laser with SPF, which removes a portion of the cladding to form a polished region; propagated light confined in the core can escape out to this polished surface via evanescent waves, giving rise to strong interactions between light and the external environment. The responses of different types of fibre-optic humidity sensors are listed in Table 11. It is found that the MoS$_2$-coated SPF sensor has a high response, and the MoS$_2$-coated ESMF has a fast response time, which enables the fibre-optic sensor to monitor different breathing patterns of human beings. The impedance and capacitive humidity sensors are listed in Table 12. All of them show ultra-high sensing response, for instance, the sensing response of SmFeO$_3$-modified MoS$_2$ nanocomposites is more than five orders of magnitude (10 598 100%) within the whole RH range of 11% to 95% RH at 10 Hz. Moreover, the combination of a polymeric material, poly(3,4-ethylenedioxythiophene) polystyrene sulfonate (PEDOT:PSS), and MoS$_2$ 2D NFKs gives a humidity sensor with an ultra-fast response and excellent recovery with values of 0.5 s and 0.8 s, respectively.

All the mentioned metal sulfide-based humidity sensors can work at room temperature, leading to wearable electronics applications. Among these four types of humidity sensors, fibre-

Table 12 Comparison of different metal sulfide-based humidity sensors

Material	Structure	Synthesis method	Type	RH range (%)	Response (%) or Sensitivity	τ_s/τ_r	OT (°C)	Ref.
SnS	Nanoflakes	LPE	Resistive	3–99	2 491 000 (99% RH)	6 s/4 s	RT	71
WS$_2$	Thin film	CVD	Resistive	25–90	235 600* (90% RH)	~5 s/~6 s	RT	232
ReS$_2$	Nanosheets	CVD	Resistive	30–80	600 (70% RH)	20 s/10 s	RT	234
VS$_2$	Nanosheets	LPE	Resistive	0–90	2900* (90% RH)	30–40 s/12–50 s	RT	233
Pt–MoS$_2$	NFKs	Solution methods	Resistive	35–85	400 000 (85% RH)	91.2 s/153.6 s	RT	235
TaS$_2$	Nanosheets	CVD	Impedance	11–95	20 190 (11% RH)	0.6 s/2 s	RT	238
MoS$_2$	Nanospheres	Hydrothermal method	Capacitive	17.2–89.5	81.9 pF/% RH (sensitivity)	140 s/80 s	RT	239
MoS$_2$	QDs	LPE	Impedance	10–95	2.21 MΩ/% RH (sensitivity)	14 s	RT	240
MoS$_2$/VS$_2$	Nanocomposite	Hydrothermal method	Impedance	11–95	579 750* (95% RH)	23 s/13 s	RT	35
MoS$_2$/ZnO	Nanocomposites	Hydrothermal & chemical method	Impedance	11–95	—	1 s/20 s	RT	241
MoS$_2$/Ag	Nanocomposites	Mixture dispersion	Capacitive	11–97	21 112 pF/% RH (sensitivity)	~1.5 s	RT	242
MoS$_2$/SnO$_2$	Nanocomposite	Hydrothermal method	Capacitive	0–97	3 285 000 (97% RH)	5/13 s	RT	243
SmFeO$_3$@MoS$_2$	Nanocomposites	Hydrothermal method	Impedance	11–95	10 598 100* (95% RH)	1.5 s/29.8 s	RT	244
PEDOT:PSS/MoS$_2$	Nanocomposites	Exfoliation & deposition	Impedance	0–80	50 kΩ/% RH, 850 Hz/% RH (sensitivity)	0.5 s/0.8 s	RT	245
SnS$_2$/GO	Nanocomposites	Solvothermal method, mixture	Impedance	11–97	6 539 600 (97% RH)	0.9 s/10 s	RT	246
SnS$_2$/TiO$_2$	Nanohybrid film	LBL self-assembly	Impedance	11–97	442 000 Ω/% RH (sensitivity)	<58 s	RT	247
SnS$_2$/Zn$_2$SnO$_4$	Nanohybrid	Solvothermal method	Capacitive	0–97	10 709 pF/% RH (sensitivity)	18 s/1 s	RT	248
ZnO NDs/WS$_2$	Heterostructure	Evaporation	Capacitive	18–85	101.71 fF/% RH (sensitivity)	74.51 s/25.67 s	RT	249
WS$_2$/SnO$_2$	Nanocomposites	LBL self-assembly	Capacitive	11–97	14 125 900 (97% RH) 21 112 pF/% RH (sensitivity)	100 s/100 s	RT	250

24968 | J. Mater. Chem. A, 2020, **8**, 24943–24976

This journal is © The Royal Society of Chemistry 2020

optic sensors have ultrafast response speed and low response and a complex measurement setup. However, it is necessary to find a way to easily integrate the fibre-optic sensor into one package that can be used for gas testing. Besides, humidity sensors can not only be used to monitor the patient's respiration profile continuously but also to determine the dehydration state. Highly sensitive and fast response and recovery humidity sensors are urgently required in real-world applications.

5. Summary and perspectives

This review shows a systematic summary of the crystal structure and gas sensing mechanism of metal sulfide nanomaterials, as well as the gas-sensing performance of metal sulfide-based devices. Here, to summarise the state-of-the-art metal sulfide gas sensors and analyse future and perspectives of the metal sulfide sensor market, we further provide a brief Strengths–Weaknesses–Opportunities–Threats (SWOT) analysis of metal sulfide technology for gas sensing.

5.1 Strengths

(1) Mechanism analysis. This is an efficient way to analyze and predict the gas sensing properties by combining theoretical (DFT) and experimental (i.e., materials characterization and gas testing) methods. For instance, the higher the adsorption energy, the higher the selectivity toward this kind of gas molecule; the ELF plot can reflect the chemical bond between the gas molecule and metal sulfides, which affect the nature of physisorption and chemisorption and further influence the recovery time of the device; the charge transfer between the gases and metal sulfides can reveal the donor or acceptor of the gases, which is associated with the change of conductivity.

(2) Improvements in gas sensing performance.

(i) Functionalization of metal sulfides. To further improve the sensitivity, doping and defect substitution are the most commonly used tools in functionalization and are efficient methods to change the band structure, modify the electronic and transport properties, and enhance the gas sensing applications. However, most of the gas sensing behaviours of functionalized metal sulfides were analyzed through DFT calculations. There are a lack of experimental reports on the influence of defects on the metal sulfide-based devices' gas-sensing performance.

(ii) Schottky junction and heterojunction gas sensors. They are based on band alignment theory, which can significantly improve the gas sensing response and LOD. Most of them have excellent sensing performances, including high response, fast response time, wide detection range, and low LOD. Thus, more people are focusing on junction-based gas sensors.

(iii) FET gas sensors. Most FET gas sensors ultimately modify the sensitivity towards a target gas by changing the energy landscape of the sensor surface. This type of sensing device has been used to detect many types of gases, such as CO, NO, NH_3, NO_2, SO_2, H_2, and VOCs. However, most of the FET gas sensors are still not satisfactory in the aspects of device instability and

limited large-scale production, even though they have a fast response and selectivity.

(iv) Other sensing mechanisms. The optical gas sensor has been employed to detect non-polar gases, such as CH_4, due to its high accuracy. Most of them are fibre optic gas sensors based on the reduction in the effective refractive index and showed high selectivity to methanol among VOCs. SAW gas sensors can detect a low concentration of NO_2 gas at room temperature with good efficiency and selectivity, and they are coated with polymers for the identification of breath biomarkers and the diagnosis of various diseases.

(3) Applications. Suitable applications for each type of gas sensor are found according to the specific gas-sensing performance of various metal sulfides. It is found that the IV–VI compound pristine metal sulfides, such as SnS, PbS, and GeS, show fast response and recovery time. The II–VI compound semiconductors, such as CdS and ZnS, have high response and selectivity to VOCs. However, most of their OTs are relatively high. Most of the transition metal sulfides have a larger electronegativity, potentially increasing the number of gas adsorption sites, and have been used for gas sensing of NO_x, NH_3, O_2, and ethanol. With respect to VOCs, various pristine metal sulfides can be used for the detection of acetone, while functionalized or heterojunction-based metal sulfides are applied for sensing benzene, methane, formaldehyde, ethanol, and LPG. Most of them work at low temperatures, except for the detection of ethanol, whose OT is usually higher than 150 °C. In the aspect of inorganic gases, all types of metal sulfides are used for sensors. Heterojunction-based and FET-based metal sulfide devices are promising candidates for gas sensing. They can take advantage of metal sulfide and other materials (such as metal, dissimilar metal sulfide, metal oxide, and organic materials) as well as the field-effect induced by back gate bias. The large surface to volume ratio combined with significant changes in the measured signals upon gas adsorption induce high sensitivity and selectivity and low LOD. Besides, to improve their performance, researchers used light illumination to stimulate the charge transfer between the gas molecules and metal sulfide.[251] Thus, the light source can be integrated into the device in the future.

5.2 Weaknesses

(1) Lack of a low LOD. Biomarkers, such as NO_x, NH_3, and CH_4, are at hundreds or tens of ppb in people. It is challenging to detect lung diseases, i.e., asthma, by the detection of NO_x in exhaled breath. MoS_2/ZnO has the lowest LOD for NH_3, which is 12 ppb. $Au/Gr–MoS_2–Gr/Au$ can detect 0.1 ppb NO_2, and Ni-doped MoS_2 can detect 250 ppb SO_2. For VOCs, $\alpha\text{-}Fe_2O_3/MoS_2$ has a LOD of 1 ppm toward ethanol at room temperature. However, it is not as low as the LOD requirement for biomarker detection.

(2) Insufficient gas selectivity. Most gas testing reported in previous work was conducted in dry atmospheres. In contrast, the working environment may be under high humidity conditions in the real world; for instance, exhaled human breath contains almost saturated moisture; the RH level is higher in

This journal is © The Royal Society of Chemistry 2020

J. Mater. Chem. A, 2020, 8, 24943–24976 | 24969

the basin area. This thereby affects the sensitivity and selectivity of sensors. The effect of humidity could be reduced significantly by using a moisture absorber, increasing the OT, or optimizing the morphology or architecture of the materials. However, it is challenging to distinguish the specified concentration of the target gas in a mixture. For instance, the automobile exhaust pollutants primarily include CO, hydrocarbons, NO, SO_2, particles (*i.e.*, some lead compounds, oil mist, and heavy metal compounds), and odour (*i.e.*, formaldehyde). The large-sized particles may cover the surface of the material and further affect the response to NO, CO, or SO_2. Similarly, in the aspect of lung cancer detection, because there is no single biomarker for lung cancer, it is much more difficult than detecting asthma, diabetes, and halitosis. More work needs to be done in this field.

(3) Lack of reproducibility. 2D/nanostructured metal sulfides have large surface areas and abundant adsorption sites, which possess high adsorption energies towards gas molecules, especially chemisorbed gases. It is challenging to desorb them from the metal sulfides without external stimulation (high temperature, high bias voltage, or light illumination). There-fore, the devices could not be recovered to the initial state. Besides, the experimental conditions are hard to reproduce, and there are a lack of standardized methods to carry out the testing. Moreover, the absence of standardization, quality assurance, and reliable benchmarking are still crucial issues that hinder the applications of metal sulfides in the healthcare area.

(4) Lack of precise mechanism analysis. Most of the reported mechanisms are analyzed through DFT calculations. Some-times, the simulation model cannot consider every detail shown in the experiment, which induces deviations between the simulation and experimental results. It is necessary to find an efficient tool or method to realize the benchmark.

All metal sulfide-based devices face the same problem as all solid-state sensors, such as translation from academic to industrial research, reproducibility of the lab conditions, batch production, integration/communication/power supply and real-world detection.

5.3 Opportunities

(1) New nanomaterials are emerging. Nanostructured metal sulfides with different forms, such as nanowires, nanoflowers, nanopores, and nanorods; or combined with hybrid materials, *e.g.*, materials decorated with metal or semiconductor particles, Schottky junctions with a metal layer or CNMs, and hetero-structures with hBN, MXene, and MOFs; or those using novel substrates, such as PVP, PI, PDMS, and other flexible substrates, can help to realize skin patching of human beings or can be integrated into a textile.

(2) The matching between materials and circuit electrodes, such as the energy band and work function, needs to be considered in terms of device design. Meanwhile, real-time detection applications, signal processing, low energy consumption, intelligent operation, and integration with sensor networks (*e.g.*, internet of things) need to be considered. The

combinations of 2D gas sensors with artificial intelligence in smart cities, smart homes, and smart hospitals are hot topics for the future.

(3) FET devices can effectively improve the gas sensing performance, but it is necessary to control their energy consumption and turn-on voltage reasonably in the future. Device performance can be enhanced by designing the device structure (shape and size of gate-drain electrodes), selecting the dielectric layer, and selecting the substrate. Some metal sulfides (such as MoS_2 and WS_2) could play an important role in elec-tronics for logic, memory, and connections, enabling the extension of Moore's law,[252] as well as the Paradigm of "More than Moore".[253,254] There are primarily three challenges for these materials to meet industry needs in practical devices, such as the accuracy of the predicting properties, the methods of growing and testing high-quality materials, and the assessment of the device's performance.

5.4 Threats

The improvements of metal sulfide-based nanomaterials and other nanotechnologies in the gas-sensing performance are still being analyzed. The equipment used for the nanomaterial-based device should be different from those for traditional Si-based devices. For the future, the application of new nano-material devices still has a long way to go. For example, the current of the metal sulfide device is too small, and it is necessary to implement signal acquisition and intelligent control through a precise amplifier circuit. Defective materials are difficult to desorb, and additional UV light sources are needed to achieve rapid desorption, increasing the overall size and cost of the device. Time will be needed to reach market readiness and to overcome the reluctance to accept and intro-duce new technology, which now remains a severe hindrance in incorporating the production chain.

In this review, we listed the latest progress made in improving the field of 2D-metal sulfide-based gas sensors to overview the developments seen in this area extending from crystal features to device engineering. The crystal structures of metal sulfides and the gas sensing mechanism based on DFT analysis are introduced first. Various types of metal sulfide-based gas-sensing devices, including chemiresistors, functionalized-metal sulfides, Schottky diodes, hetero-junctions, field-effect transistors, and optical, impedance, capacitive and SAW sensors, are compared and presented. We then discuss the extensive applications of metal sulfide-based sensors in gas sensing. Various gas sensors for the detection of VOC biomarkers (*e.g.*, acetone, benzene, methane, formal-dehyde, and ethanol) and inorganic gases (*e.g.*, CO_2, NH_3, H_2S, NO, and humidity) were discussed. There is a fabulous oppor-tunity right now for developing 2D metal sulfides as gas sensors and use them for gas sensing, even integrated into the IoT system. However, they still have some shortcomings that need to be overcome, such as a high LOD, effect of a high humidity environment, insufficient gas selectivity, and low reproduc-ibility in gas detection. It is necessary to develop new materials or construct advanced nanostructures to improve the

24970 | *J. Mater. Chem. A*, 2020, **8**, 24943–24976

This journal is © The Royal Society of Chemistry 2020

performances. Additionally, from a device architecture perspective, implementation of the new signal-processing technology and recognition algorithms based on a single-chip system using multiplex detection channels is a significant and promising route for the development of gas sensing platforms.

Conflicts of interest

The authors declare no conflict of interest.

References

1 J. Zhang, X. Liu, G. Neri and N. Pinna, *Adv. Mater.*, 2016, **28**, 795–831.

2 A. Afroozeh, E. Akbari and P. Yupapin, *J. Nanoelectron. Optoelectron.*, 2019, **14**, 1225–1229.

3 S. Feng, F. Farha, Q. Li, Y. Wan, Y. Xu, T. Zhang and H. Ning, *Sensors*, 2019, **19**, 3760.

4 S. Das and M. Pal, *J. Electrochem. Soc.*, 2020, **167**, 037562.

5 S. Orzechowska, A. Mazurek, R. Świsłocka and W. Lewandowski, *Materials*, 2019, **13**, 80.

6 A. Roine, E. Veskimäe, A. Tuokko, P. Kumpulainen, J. Koskimäki, T. A. Keinänen, M. R. Häkkinen, J. Vepsäläinen, T. Paavonen, J. Lekkala, T. Lehtimäki, T. L. Tammela and N. K. J. Oksala, *J. Urol.*, 2014, **192**, 230–235.

7 J.-C. Juncker, *Official Journal of the European Union*, 2017, **6**, 115–120, https://eur-lex.europa.eu/legal-content/EN/TXT/?uri=uriserv%3AOJ.L_.2017.027.01.0115.01.ENG.

8 D. J. Buckley, N. C. G. Black, E. G. Castanon, C. Melios, M. Hardman and O. Kazakova, *2D Mater.*, 2020, **7**, 032002.

9 G. Korotcenkov, *Mater. Sci. Eng., B*, 2007, **139**, 1–23.

10 Y. Pang, J. Jian, T. Tu, Z. Yang, J. Ling, Y. Li, X. Wang, Y. Qiao, H. Tian, Y. Yang and T.-L. Ren, *Biosens. Bioelectron.*, 2018, **116**, 123–129.

11 L. Sacco, S. Forel, I. Florea and C.-S. Cojocaru, *Carbon*, 2020, **157**, 631–639.

12 V. Schroeder, S. Savagatrup, M. He, S. Lin and T. M. Swager, *Chem. Rev.*, 2019, **119**, 599–663.

13 H. T. Kim, H. Y. Kim, Y. S. Park, Y. S. Kim and W. H. Jang, *Chemosensors*, 2017, **5**, 15.

14 N. Taguchi, Japanese patent, 4538200, 1962.

15 W.-T. Koo, S.-J. Choi, N.-H. Kim, J.-S. Jang and I.-D. Kim, *Sens. Actuators, B*, 2016, **223**, 301–310.

16 D. Kwak, M. Wang, K. J. Koski, L. Zhang, H. Sokol, R. Maric and Y. Lei, *ACS Appl. Mater. Interfaces*, 2019, **11**, 10697–10706.

17 J.-S. Jang, S.-J. Choi, S.-J. Kim, M. Hakim and I.-D. Kim, *Adv. Funct. Mater.*, 2016, **26**, 4740–4748.

18 W. Liu, L. Xu, K. Sheng, X. Zhou, B. Dong, G. Lu and H. Song, *NPG Asia Mater.*, 2018, **10**, 293–308.

19 Y. Chen, L. Yu, Q. Li, Y. Wu, Q. Li and T. Wang, *Nanotechnology*, 2012, **23**, 415501.

20 Y. Deng, *Semiconducting Metal Oxides for Gas Sensing*, Springer, 2019.

21 E. Gabal, S. Chatterjee, F. K. Ahmed and K. A. Abd-Elsalam, in *Carbon Nanomaterials for Agri-Food and Environmental Applications*, ed. K. A. Abd-Elsalam, Elsevier, 2020, pp. 133–153, DOI: 10.1016/B978-0-12-819786-8.00007-4.

22 C. R. Minitha, V. S. Anithaa, V. Subramaniam and R. T. Rajendra Kumar, *ACS Omega*, 2018, **3**, 4105–4112.

23 R. Sha, S. K. Puttapati, V. V. S. S. Srikanth and S. Badhulika, *J. Electroanal. Chem.*, 2017, **785**, 26–32.

24 S. Kubendhiran, S. Sakthinathan, S.-M. Chen, P. Tamizhdurai, K. Shanthi and C. Karuppiah, *J. Colloid Interface Sci.*, 2017, **497**, 207–216.

25 F. Rigoni, S. Tognolini, P. Borghetti, G. Drera, S. Pagliara, A. Goldoni and L. Sangaletti, *Analyst*, 2013, **138**, 7392–7399.

26 E. Singh, M. Meyyappan and H. S. Nalwa, *ACS Appl. Mater. Interfaces*, 2017, **9**, 34544–34586.

27 E. Lee, Y. S. Yoon and D.-J. Kim, *ACS Sens.*, 2018, **3**, 2045–2060.

28 C.-H. Lai, M.-Y. Lu and L.-J. Chen, *J. Mater. Chem.*, 2012, **22**, 19–30.

29 M. Donarelli, S. Prezioso, F. Perrozzi, F. Bisti, M. Nardone, L. Giancaterini, C. Cantalini and L. Ottaviano, *Sens. Actuators, B*, 2015, **207**, 602–613.

30 Z. Tian, C. Guo, M. Zhao, R. Li and J. Xue, *ACS Nano*, 2016, **11**, 2219.

31 A. S. Rodin, L. C. Gomes, A. Carvalho and A. H. Castro Neto, *Phys. Rev. B*, 2016, **93**, 045431.

32 S. Zhang, N. Wang, S. Liu, S. Huang, W. Zhou, B. Cai, M. Xie, Q. Yang, X. Chen and H. Zeng, *Nanotechnology*, 2016, **27**, 274001.

33 J. Wang, G. Lian, Z. Xu, C. Fu, Z. Lin, L. Li, Q. Wang, D. Cui and C.-P. Wong, *ACS Appl. Mater. Interfaces*, 2016, **8**, 9545–9551.

34 M. F. Afsar, M. A. Rafiq and A. I. Y. Tok, *RSC Adv.*, 2017, **7**, 21556–21566.

35 X. Chen, K. Yu, Y. Shen, Y. Feng and Z. Zhu, *ACS Appl. Mater. Interfaces*, 2017, **9**, 42139–42148.

36 W. Zhou, X. Zou, S. Najmaei, Z. Liu, Y. Shi, J. Kong, J. Lou, P. M. Ajayan, B. I. Yakobson and J.-C. Idrobo, *Nano Lett.*, 2013, **13**, 2615–2622.

37 J. Zhu, H. Zhang, Y. Tong, L. Zhao, Y. Zhang, Y. Qiu and X. Lin, *Appl. Surf. Sci.*, 2017, **419**, 522–530.

38 F. K. Perkins, A. L. Friedman, E. Cobas, P. M. Campbell, G. G. Jernigan and B. T. Jonker, *Nano Lett.*, 2013, **13**, 668–673.

39 Z. Ashkavand, E. Sadeghi, R. Parvizi and M. Zare, *ACS Appl. Mater. Interfaces*, 2020, **12**, 34283–34296.

40 S. Chandrasekaran, L. Yao, L. Deng, C. Bowen, Y. Zhang, S. Chen, Z. Lin, F. Peng and P. Zhang, *Chem. Soc. Rev.*, 2019, **48**, 4178–4280.

41 Y. Cui, Z. Zhou, T. Li, K. Wang, J. Li and Z. Wei, *Adv. Funct. Mater.*, 2019, **29**, 1900040.

42 S. Manzeli, D. Ovchinnikov, D. Pasquier, O. V. Yazyev and A. Kis, *Nat. Rev. Mater.*, 2017, **2**, 17033.

43 W. Choi, N. Choudhary, G. H. Han, J. Park, D. Akinwande and Y. H. Lee, *Mater. Today*, 2017, **20**, 116–130.

44 J. Ping, Z. Fan, M. Sindoro, Y. Ying and H. Zhang, *Adv. Funct. Mater.*, 2017, **27**, 1605817.

45 Z. Xie, D. Wang, T. Fan, C. Xing, Z. Li, W. Tao, L. Liu, S. Bao, D. Fan and H. Zhang, *J. Mater. Chem. B*, 2018, **6**, 4747–4755.

This journal is © The Royal Society of Chemistry 2020

J. Mater. Chem. A, 2020, **8**, 24943–24976 | 24971

46 S. Kouser, A. Thannikoth, U. Gupta, U. V. Waghmare and C. N. R. Rao, *Small*, 2015, **11**, 4723–4730.

47 R. M. Martin, *Phys. Rev. B: Solid State*, 1970, **1**, 4005–4011.

48 V. Lantto and V. Golovanov, *Sens. Actuators, B*, 1995, **25**, 614–618.

49 Y. Rodríguez-Lazcano, H. Martínez, M. Calixto-Rodríguez and A. Núñez Rodríguez, *Thin Solid Films*, 2009, **517**, 5951–5955.

50 D. G. Bell, D. M. Hum, L. Pincherle, D. W. Sciama, P. M. Woodward and N. F. Mott, *Proc. R. Soc. London, Ser. A*, 1953, **217**, 71–91.

51 J. Tian and G. Cao, *Nano Rev.*, 2013, **4**, 22578.

52 J. Trahan, R. G. Goodrich and S. F. Watkins, *Phys. Rev. B: Solid State*, 1970, **2**, 2859–2863.

53 Z. Wang, S. Ning, T. Fujita, A. Hirata and M. Chen, *ACS Nano*, 2016, **10**, 10308–10316.

54 A. Splendiani, L. Sun, Y. Zhang, T. Li, J. Kim, C.-Y. Chim, G. Galli and F. Wang, *Nano Lett.*, 2010, **10**, 1271–1275.

55 T. A. J. Loh and D. H. C. Chua, *J. Phys. Chem. C*, 2015, **119**, 27496–27504.

56 L. A. Burton, D. Colombara, R. D. Abellon, F. C. Grozema, L. M. Peter, T. J. Savenije, G. Dennler and A. Walsh, *Chem. Mater.*, 2013, **25**, 4908–4916.

57 L. Li, X. Fang, T. Zhai, M. Liao, U. K. Gautam, X. Wu, Y. Koide, Y. Bando and D. Golberg, *Adv. Mater.*, 2010, **22**, 4151–4156.

58 K. Xu, Z. Wang, F. Wang, Y. Huang, F. Wang, L. Yin, C. Jiang and J. He, *Adv. Mater.*, 2015, **27**, 7881–7887.

59 Y. Kim, K. C. Kwon, S. Kang, C. Kim, T. H. Kim, S.-P. Hong, S. Y. Park, J. M. Suh, M.-J. Choi, S. Han and H. W. Jang, *ACS Sens.*, 2019, **4**, 2395–2402.

60 Q. He, Q. Ma, B. Chen, Z. Yin, Z. Zeng, S. Wu, X. Cao, X. Kong and H. Zhang, *APL Mater.*, 2014, **2**, 092506.

61 S. Liu, W. Xiao, M. Zhong, L. Pan, X. Wang, H.-X. Deng, J. Liu, J. Li and Z. Wei, *Nanotechnology*, 2018, **29**, 184002.

62 N. Rafiefard, A. Iraji zad, A. Esfandiar, P. Sasanpour, S. Fardindoost, Y. Zou, S. J. Haigh and S. H. H. Shokouh, *Microchim. Acta*, 2020, **187**, 117.

63 Y.-R. Tao, X.-C. Wu and W.-W. Xiong, *Small*, 2014, **10**, 4905–4911.

64 W.-W. Xiong, J.-Q. Chen, X.-C. Wu and J.-J. Zhu, *J. Mater. Chem. C*, 2014, **2**, 7392–7395.

65 C. C. Mayorga-Martinez, Z. Sofer, J. Luxa, Š. Huber, D. Sedmidubský, P. Brázda, L. Palatinus, M. Mikulics, P. Lazar, R. Medlín and M. Pumera, *ACS Nano*, 2018, **12**, 464–473.

66 W. Huang, L. Gan, H. Yang, N. Zhou, R. Wang, W. Wu, H. Li, Y. Ma, H. Zeng and T. Zhai, *Adv. Funct. Mater.*, 2017, **27**, 1702448.

67 U. G. E. Perera, H. J. Kulik, V. Iancu, L. G. G. V. Dias da Silva, S. E. Ulloa, N. Marzari and S. W. Hla, *Phys. Rev. Lett.*, 2010, **105**, 106601.

68 C. Xu, X. Huang, X. Xu, X. Zhang and H. Zhang, *Int. J. Quantum Chem.*, 2020, **120**, e26120.

69 A. Savin, R. Nesper, S. Wengert and T. F. Fässler, *Angew. Chem., Int. Ed. Engl.*, 1997, **36**, 1808–1832.

70 J. K. Burdett and T. A. McCormick, *J. Phys. Chem. A*, 1998, **102**, 6366–6372.

71 H. Tang, Y. Li, H. Ye, f. Hu, C. Gao, L.-Q. Tao, T. Tu, G. Gou, X. Chen, X. Fan, T.-L. Ren and G. Zhang, *Nanotechnology*, 2019, **31**, 055501.

72 F. Hu, H. Tang, C. Tan, H. Ye, X. Chen and G. Zhang, *IEEE Electron Device Lett.*, 2017, **38**, 983–986.

73 S.-J. Choi and I.-D. Kim, *Electron. Mater. Lett.*, 2018, **14**, 221–260.

74 Q. Yue, Z. Shao, S. Chang and J. Li, *Nanoscale Res. Lett.*, 2013, **8**, 425.

75 S. Zhao, J. Xue and W. Kang, *Chem. Phys. Lett.*, 2014, **595–596**, 35–42.

76 J. Cha, K.-A. Min, D. Sung and S. Hong, *Curr. Appl. Phys.*, 2018, **18**, 1013–1019.

77 S. Ma, D. Yuan, Y. Wang and Z. Jiao, *J. Mater. Chem. C*, 2018, **6**, 8082–8091.

78 D. B. Putungan, S.-H. Lin and J.-L. Kuo, *Phys. Chem. Chem. Phys.*, 2015, **17**, 21702–21708.

79 Y. Linghu and C. Wu, *J. Phys. Chem. C*, 2019, **123**, 10339–10345.

80 Q. Tang and D.-e. Jiang, *Chem. Mater.*, 2015, **27**, 3743–3748.

81 Z. Qin, D. Zeng, J. Zhang, C. Wu, Y. Wen, B. Shan and C. Xie, *Appl. Surf. Sci.*, 2017, **414**, 244–250.

82 H. Li, Z. Yin, Q. He, H. Li, X. Huang, G. Lu, D. W. H. Fam, A. I. Y. Tok, Q. Zhang and H. Zhang, *Small*, 2012, **8**, 63–67.

83 D. J. Late, Y.-K. Huang, B. Liu, J. Acharya, S. N. Shirodkar, J. Luo, A. Yan, D. Charles, U. V. Waghmare, V. P. Dravid and C. N. R. Rao, *ACS Nano*, 2013, **7**, 4879–4891.

84 Y. Li, X. Zhang, D. Chen, S. Xiao and J. Tang, *Appl. Surf. Sci.*, 2018, **443**, 274–279.

85 H. Luo, Y. Cao, J. Zhou, J. Feng, J. Cao and H. Guo, *Chem. Phys. Lett.*, 2016, **643**, 27–33.

86 H. Wei, Y. Gui, J. Kang, W. Wang and C. Tang, *Nanomaterials*, 2018, **8**, 646.

87 A. Sharma, Anu, M. S. Khan, M. Husain, M. S. Khan and A. Srivastava, *IEEE Sens. J.*, 2018, **18**, 2853–2860.

88 D. Ma, W. Ju, T. Li, X. Zhang, C. He, B. Ma, Z. Lu and Z. Yang, *Appl. Surf. Sci.*, 2016, **383**, 98–105.

89 R. Zhang, D. Fu, J. Ni, C. Sun and S. Song, *Chem. Phys. Lett.*, 2019, **715**, 273–277.

90 D. Zhang, J. Wu, P. Li and Y. Cao, *J. Mater. Chem. A*, 2017, **5**, 20666–20677.

91 Y. Kadioglu, G. Gökoğlu and O. Üzengi Aktürk, *Appl. Surf. Sci.*, 2017, **425**, 246–253.

92 V. Q. Bui, T.-T. Pham, D. A. Le, C. M. Thi and H. M. Le, *J. Phys.: Condens. Matter*, 2015, **27**, 305005.

93 C. Zhou, W. Yang and H. Zhu, *J. Chem. Phys.*, 2015, **142**, 214704.

94 B. Zhao, C. Shang, N. Qi, Z. Y. Chen and Z. Q. Chen, *Appl. Surf. Sci.*, 2017, **412**, 385–393.

95 F. Li and C. Shi, *Appl. Surf. Sci.*, 2018, **434**, 294–306.

96 J. M. Jasmine, A. Aadhityan, C. Preferencial kala and D. J. Thiruvadigal, *Appl. Surf. Sci.*, 2019, **489**, 841–848.

97 H. Li, M. Huang and G. Cao, *Phys. Chem. Chem. Phys.*, 2016, **18**, 15110–15117.

98 L. A. Currie, *Anal. Chim. Acta*, 1999, **391**, 105–126.

24972 | *J. Mater. Chem. A*, 2020, **8**, 24943–24976

This journal is © The Royal Society of Chemistry 2020

99 J. Burgués, J. M. Jiménez-Soto and S. Marco, *Anal. Chim. Acta*, 2018, **1013**, 13–25.

100 S. T. Navale, D. K. Bandgar, M. A. Chougule and V. B. Patil, *RSC Adv.*, 2015, **5**, 6518–6527.

101 H. Liu, M. Li, G. Shao, W. Zhang, W. Wang, H. Song, H. Cao, W. Ma and J. Tang, *Sens. Actuators, B*, 2015, **212**, 434–439.

102 X.-H. Liu, P.-F. Yin, S. A. Kulinich, Y.-Z. Zhou, J. Mao, T. Ling and X.-W. Du, *ACS Appl. Mater. Interfaces*, 2017, **9**, 602–609.

103 X. Wang, Z. Xie, H. Huang, Z. Liu, D. Chen and G. Shen, *J. Mater. Chem.*, 2012, **22**, 6845–6850.

104 F. A. Sabah, N. M. Ahmed, Z. Hassan and H. S. Rasheed, *Sens. Actuators, A*, 2016, **249**, 68–76.

105 E. C. Linganiso, B. W. Mwakikunga, S. D. Mhlanga, N. J. Coville, B. T. Sone and M. Maaza, *Sensors*, 2012, 1–4.

106 N. Souda and Y. Shimizu, *J. Mater. Sci.*, 2003, **38**, 4301–4305.

107 D.-H. Baek and J. Kim, *Sens. Actuators, B*, 2017, **250**, 686–691.

108 A. A. Ramanathan, *IOP Conf. Ser.: Mater. Sci. Eng.*, 2018, **305**, 012001.

109 Z. Qin, K. Xu, H. Yue, H. Wang, J. Zhang, C. Ouyang, C. Xie and D. Zeng, *Sens. Actuators, B*, 2018, **262**, 771–779.

110 R. T. Tung, *Appl. Phys. Rev.*, 2014, **1**, 011304.

111 Y. Kim, S.-K. Kang, N.-C. Oh, H.-D. Lee, S.-M. Lee, J. Park and H. Kim, *ACS Appl. Mater. Interfaces*, 2019, **11**, 38902–38909.

112 V. Van Quang, N. Van Dung, N. Sy Trong, N. Duc Hoa, N. Van Duy and N. Van Hieu, *Appl. Phys. Lett.*, 2014, **105**, 013107.

113 X. Zheng, A. Calò, E. Albisetti, X. Liu, A. S. M. Alharbi, G. Arefe, X. Liu, M. Spieser, W. J. Yoo, T. Taniguchi, K. Watanabe, C. Aruta, A. Ciarrocchi, A. Kis, B. S. Lee, M. Lipson, J. Hone, D. Shahrjerdi and E. Riedo, *Nat. Electron.*, 2019, **2**, 17–25.

114 T. Pham, G. Li, E. Bekyarova, M. E. Itkis and A. Mulchandani, *ACS Nano*, 2019, **13**, 3196–3205.

115 M.-L. Tsai, S.-H. Su, J.-K. Chang, D.-S. Tsai, C.-H. Chen, C.-I. Wu, L.-J. Li, L.-J. Chen and J.-H. He, *ACS Nano*, 2014, **8**, 8317–8322.

116 T. Ihn, *Semiconductor Nanostructures: Quantum States and Electronic Transport*, Oxford University Press, 2010.

117 K. Xu, N. Li, D. Zeng, S. Tian, S. Zhang, D. Hu and C. Xie, *ACS Appl. Mater. Interfaces*, 2015, **7**, 11359–11368.

118 X. Wang, L. Huang, Y. Peng, N. Huo, K. Wu, C. Xia, Z. Wei, S. Tongay and J. Li, *Nano Res.*, 2016, **9**, 507–516.

119 H. Yan, P. Song, S. Zhang, Z. Yang and Q. Wang, *RSC Adv.*, 2015, **5**, 79593–79599.

120 X.-Q. Qiao, Z.-W. Zhang, D.-F. Hou, D.-S. Li, Y. Liu, Y.-Q. Lan, J. Zhang, P. Feng and X. Bu, *ACS Sustainable Chem. Eng.*, 2018, **6**, 12375–12384.

121 Y. Han, Y. Ma, Y. Liu, S. Xu, X. Chen, M. Zeng, N. Hu, Y. Su, Z. Zhou and Z. Yang, *Appl. Surf. Sci.*, 2019, **493**, 613–619.

122 X. Wang, Y. Sang, D. Wang, S. Ji and H. Liu, *J. Alloys Compd.*, 2015, **639**, 571–576.

123 S. Park, S. An, Y. Mun and C. Lee, *ACS Appl. Mater. Interfaces*, 2013, **5**, 4285–4292.

124 W. Zeng, Y. Liu, J. Mei, C. Tang, K. Luo, S. Li, H. Zhan and Z. He, *Sens. Actuators, B*, 2019, **301**, 127010.

125 A. Katoch, J.-H. Kim and S. S. Kim, *ACS Appl. Mater. Interfaces*, 2014, **6**, 21494–21499.

126 G.-J. Sun, J. K. Lee, S. Choi, W. I. Lee, H. W. Kim and C. Lee, *ACS Appl. Mater. Interfaces*, 2017, **9**, 9975–9985.

127 E. Espid and F. Taghipour, *Sens. Actuators, B*, 2017, **241**, 828–839.

128 Z. Li, Y. Liu, D. Guo, J. Guo and Y. Su, *Sens. Actuators, B*, 2018, **271**, 306–310.

129 Q. Zhang, S. Ma, R. Zhang, K. Zhu, Y. Tie and S. Pei, *J. Alloys Compd.*, 2019, **807**, 151650.

130 M. Li, W. Ren, R. Wu and M. Zhang, *Sensors*, 2017, **17**, 1577.

131 J. Zhai, L. Wang, D. Wang, H. Li, Y. Zhang, D. q. He and T. Xie, *ACS Appl. Mater. Interfaces*, 2011, **3**, 2253–2258.

132 D. Yang, I. Cho, D. Kim, M. A. Lim, Z. Li, J. G. Ok, M. Lee and I. Park, *ACS Appl. Mater. Interfaces*, 2019, **11**, 24298–24307.

133 S. Park, G.-J. Sun, H. Kheel, T. Ko, H. W. Kim and C. Lee, *Appl. Phys. A: Mater. Sci. Process.*, 2016, **122**, 504.

134 F. Schedin, A. K. Geim, S. V. Morozov, E. W. Hill, P. Blake, M. I. Katsnelson and K. S. Novoselov, *Nat. Mater.*, 2007, **6**, 652–655.

135 P. Bondavalli, P. Legagneux and D. Pribat, *Sens. Actuators, B*, 2009, **140**, 304–318.

136 K. S. Kim, C. H. Ahn, S. H. Jung, S. W. Cho and H. K. Cho, *ACS Appl. Mater. Interfaces*, 2018, **10**, 10185–10193.

137 B. Du, Y. Ruan, T.-T. Ly, P. Jia, Q. Sun, Q. Feng, D. Yang and H. Ebendorff-Heidepriem, *Sens. Actuators, B*, 2020, **305**, 127513.

138 D. Li, H. Lu, W. Qiu, J. Dong, H. Guan, W. Zhu, J. Yu, Y. Luo, J. Zhang and Z. Chen, *Opt. Express*, 2017, **25**, 28407–28416.

139 H. Jin, X. Tao, S. Dong, Y. Qin, L. Yu, J. Luo and M. J. Deen, *J. Micromech. Microeng.*, 2017, **27**, 115006.

140 H. Li, M. Li, H. Kan, C. Li, A. Quan, C. Fu, J. Luo, X. Liu, W. Wang, Z. Yang, Q. Wei and Y. Fu, *Surf. Coat. Technol.*, 2019, **362**, 78–83.

141 R. Atkinson, *Atmos. Environ.*, 2000, **34**, 2063–2101.

142 M. Hakim, Y. Y. Broza, O. Barash, N. Peled, M. Phillips, A. Amann and H. Haick, *Chem. Rev.*, 2012, **112**, 5949–5966.

143 J.-S. Kim, H.-W. Yoo, H. O. Choi and H.-T. Jung, *Nano Lett.*, 2014, **14**, 5941–5947.

144 L. Zhang, K. Khan, J. Zou, H. Zhang and Y. Li, *Adv. Mater. Interfaces*, 2019, 1901329.

145 H. E. Lebovitz, *Lancet*, 1995, **345**, 767–772.

146 C. Deng, J. Zhang, X. Yu, W. Zhang and X. Zhang, *J. Chromatogr. B: Anal. Technol. Biomed. Life Sci.*, 2004, **810**, 269–275.

147 A. Giberti, A. Gaiardo, B. Fabbri, S. Gherardi, V. Guidi, C. Malagù, P. Bellutti, G. Zonta, D. Casotti and G. Cruciani, *Sens. Actuators, B*, 2016, **223**, 827–833.

148 D. Gu, X. Li, Y. Zhao and J. Wang, *Sens. Actuators, B*, 2017, **244**, 67–76.

149 M. Leidinger, M. Rieger, T. Sauerwald, C. Alépée and A. Schütze, *Sens. Actuators, B*, 2016, **236**, 988–996.

This journal is © The Royal Society of Chemistry 2020

J. Mater. Chem. A, 2020, **8**, 24943–24976 | **24973**

150 World Health Organization, *WHO guidelines for indoor air quality: selected pollutants*, World Health Organization, Regional Office for Europe, Copenhagen, 2010.

151 H. Fan, Z. Peng, H. Yang and K. Zhou, *Anal. Methods*, 2016, **8**, 1257–1264.

152 C. B. Hirschmann, S. Sinisalo, J. Uotila, S. Ojala and R. L. Keiski, *Vib. Spectrosc.*, 2013, **68**, 170–176.

153 D. Zhang, C. Jiang and X. Zhou, *Talanta*, 2018, **182**, 324–332.

154 D. Zhang, J. Wu, P. Li, Y. Cao and Z. Yang, *ACS Appl. Mater. Interfaces*, 2019, **11**, 31245–31256.

155 D. Baek, K. Lee, S. Pyo, J. Choi and J. Kim, *2015 18th International Conference on Solid-State Sensors, Actuators and Microsystems (TRANSDUCERS)*, Anchorage, AK, 2015, pp. 618–621.

156 U. S. O. o. M. t. P. Earth, *Scientific Assessment of Ozone Depletion, 1994*, World Meteorological Organization, 1995.

157 A. Takahashi, Y. Urano, K. Tokuhashi, N. Hidekazu, M. Kaise and S. Kondo, *J. Loss Prev. Process Ind.*, 1998, **11**, 353–360.

158 A. J. Zehnder and T. D. Brock, *J. Bacteriol.*, 1979, **137**, 420.

159 A. Mosahebfard, H. D. Jahromi and M. H. Sheikhi, *IEEE Sens. J.*, 2016, **16**, 4174–4179.

160 H. Roshan, A. Mosahebfard and M. H. Sheikhi, *IEEE Sens. J.*, 2018, **18**, 1940–1945.

161 A. Mosahebfard, H. Roshan and M. H. Sheikhi, *IEEE Sens. J.*, 2017, **17**, 3375–3380.

162 H. Roshan, M. H. Sheikhi, M. K. F. Haghighi and P. Padidar, *IEEE Sens. J.*, 2020, **20**, 2526–2532.

163 F. Wang, H. Liu, H. Hu, Y. Li, W. Zeng and L. Zeng, *Ceram. Int.*, 2019, **45**, 22981–22986.

164 A. A. Sergeev, K. A. Sergeeva, A. A. Leonov, I. V. Postnova and S. S. Voznesenskiy, *Semiconductors*, 2018, **52**, 1846–1848.

165 S. Hussain, T. Liu, M. S. Javed, N. Aslam and W. Zeng, *Sens. Actuators, B*, 2017, **239**, 1243–1250.

166 X. Li, J. Wang, D. Xie, J. Xu, Y. Xia, W. Li, L. Xiang, Z. Li, S. Xu and S. Komarneni, *Nanotechnology*, 2017, **28**, 325501.

167 D. Zhang, C. Jiang and J. Wu, *Sens. Actuators, B*, 2018, **273**, 176–184.

168 D. Zhang, Y. Cao, Z. Yang and J. Wu, *ACS Appl. Mater. Interfaces*, 2020, **12**, 11979–11989.

169 U. S. D. O. Labor, Occupational Safety and Health Standards, in *Toxic and Hazardous Substances*, United States, 2013.

170 D. Zhang, X. Fan, A. Yang and X. Zong, *J. Colloid Interface Sci.*, 2018, **523**, 217–225.

171 A. Giberti, D. Casotti, G. Cruciani, B. Fabbri, A. Gaiardo, V. Guidi, C. Malagù, G. Zonta and S. Gherardi, *Sens. Actuators, B*, 2015, **207**, 504–510.

172 X. L. Yu, Y. Wang, H. L. W. Chan and C. B. Cao, *Microporous Mesoporous Mater.*, 2009, **118**, 423–426.

173 R. Souissi, N. Bouguila and A. Labidi, *Sens. Actuators, B*, 2018, **261**, 522–530.

174 H. Yan, P. Song, S. Zhang, Z. Yang and Q. Wang, *J. Alloys Compd.*, 2016, **662**, 118–125.

175 P. X. Zhao, Y. Tang, J. Mao, Y. X. Chen, H. Song, J. W. Wang, Y. Song, Y. Q. Liang and X. M. Zhang, *J. Alloys Compd.*, 2016, **674**, 252–258.

176 S. V. Patil, P. R. Deshmukh and C. D. Lokhande, *Sens. Actuators, B*, 2011, **156**, 450–455.

177 R. D. Ladhe, P. K. Baviskar, S. M. Pawar, J. H. Kim and B. R. Sankapal, *Sens. Actuators, A*, 2017, **267**, 187–193.

178 R. D. Ladhe, P. K. Baviskar, W. W. Tan, J. B. Zhang, C. D. Lokhande and B. R. Sankapal, *J. Phys. D: Appl. Phys.*, 2010, **43**, 245302.

179 N. B. Sonawane, P. K. Baviskar, R. R. Ahire and B. R. Sankapal, *Mater. Chem. Phys.*, 2017, **191**, 168–172.

180 N. B. Sonawane, K. V. Gurav, R. R. Ahire, J. H. Kim and B. R. Sankapal, *Sens. Actuators, A*, 2014, **216**, 78–83.

181 L. Yadava, R. Verma and R. Dwivedi, *Sens. Actuators, B*, 2010, **144**, 37–42.

182 D. S. Dhawale, D. P. Dubal, V. S. Jamadade, R. R. Salunkhe, S. S. Joshi and C. D. Lokhande, *Sens. Actuators, B*, 2010, **145**, 205–210.

183 S. Singh, A. Singh, B. C. Yadav, P. Tandon, S. Kumar, R. R. Yadav, S. I. Pomogailo, G. I. Dzhardimalieva and A. D. Pomogailo, *Sens. Actuators, B*, 2015, **207**, 460–469.

184 R. A. Michaels, *Environ. Health Perspect.*, 1999, **107**, 617–627.

185 S. E. Zohora, A. M. Khan and N. Hundewale, in *Advances in Computing and Information Technology*, Springer, Berlin, Heidelberg, 2013, vol. 178, pp. 177–184.

186 B. Liu, L. Chen, G. Liu, A. N. Abbas, M. Fathi and C. Zhou, *ACS Nano*, 2014, **8**, 5304–5314.

187 X. Li, X. Li, Z. Li, J. Wang and J. Zhang, *Sens. Actuators, B*, 2017, **240**, 273–277.

188 Y. Xiong, W. Xu, D. Ding, W. Lu, L. Zhu, Z. Zhu, Y. Wang and Q. Xue, *J. Hazard. Mater.*, 2018, **341**, 159–167.

189 N. Huo, S. Yang, Z. Wei, S.-S. Li, J.-B. Xia and J. Li, *Sci. Rep.*, 2014, **4**, 5209.

190 S. Yang, J. Kang, Q. Yue, J. M. D. Coey and C. Jiang, *Adv. Mater. Interfaces*, 2016, **3**, 1500707.

191 D. Zhang, C. Jiang and Y. e. Sun, *J. Alloys Compd.*, 2017, **698**, 476–483.

192 D. Zhang, C. Jiang, P. Li and Y. e. Sun, *ACS Appl. Mater. Interfaces*, 2017, **9**, 6462–6471.

193 S. Zhang, J. Wang, N. L. Torad, W. Xia, M. A. Aslam, Y. V. Kaneti, Z. Hou, Z. Ding, B. Da, A. Fatehmulla, A. M. Aldhafiri, W. A. Farooq, J. Tang, Y. Bando and Y. Yamauchi, *Small*, 2019, 1901718.

194 Z. Qin, C. Ouyang, J. Zhang, L. Wan, S. Wang, C. Xie and D. Zeng, *Sens. Actuators, B*, 2017, **253**, 1034–1042.

195 S. G. Leonardi, W. Wlodarski, Y. Li, N. Donato, A. Bonavita and G. Neri, *J. Alloys Compd.*, 2019, **781**, 440–449.

196 Y. Liu, L. Wang, H. Wang, M. Xiong, T. Yang and G. S. Zakharova, *Sens. Actuators, B*, 2016, **236**, 529–536.

197 T. Fu, *Sens. Actuators, B*, 2009, **140**, 116–121.

198 W. Shi, L. Huo, H. Wang, H. Zhang, J. Yang and P. Wei, *Nanotechnology*, 2006, **17**, 2918–2924.

199 B. Cho, J. Yoon, S. K. Lim, A. R. Kim, D.-H. Kim, S.-G. Park, J.-D. Kwon, Y.-J. Lee, K.-H. Lee, B. H. Lee, H. C. Ko and

24974 | *J. Mater. Chem. A*, 2020, **8**, 24943–24976

This journal is © The Royal Society of Chemistry 2020

M. G. Hahm, *ACS Appl. Mater. Interfaces*, 2015, **7**, 16775–16780.

200 S. Sharma, A. Kumar, N. Singh and D. Kaur, *Sens. Actuators, B*, 2018, **275**, 499–507.

201 C. W. Spicer, D. V. Kenny, G. F. Ward and I. H. Billick, *Air Waste*, 1993, **43**, 1479–1485.

202 A. Afzal, N. Cioffi, L. Sabbatini and L. Torsi, *Sens. Actuators, B*, 2012, **171–172**, 25–42.

203 K. Alving, E. Weitzberg and J. M. Lundberg, *Eur. Respir. J.*, 1993, **6**, 1368.

204 P. J. Barnes, R. A. Dweik, A. F. Gelb, P. G. Gibson, S. C. George, H. Grasemann, I. D. Pavord, F. Ratjen, P. E. Silkoff, D. R. Taylor and N. Zamel, *Chest*, 2010, **138**, 682–692.

205 R. K. Sonker, B. C. Yadav, V. Gupta and M. Tomar, *Mater. Chem. Phys.*, 2020, **239**, 121975.

206 S. T. Navale, A. T. Mane, M. A. Chougule, N. M. Shinde, J. Kim and V. B. Patil, *RSC Adv.*, 2014, **4**, 44547–44554.

207 V. V. Burungale, R. S. Devan, S. A. Pawar, N. S. Harale, V. L. Patil, V. K. Rao, Y. R. Ma, J. Eun Ae, J. H. Kim and P. S. Patil, *Mater. Sci.*, 2016, **34**, 204–211.

208 T. Xu, Y. Liu, Y. Pei, Y. Chen, Z. Jiang, Z. Shi, J. Xu, D. Wu, Y. Tian and X. Li, *Sens. Actuators, B*, 2018, **259**, 789–796.

209 Y.-H. Kim, D.-T. Phan, S. Ahn, K.-H. Nam, C.-M. Park and K.-J. Jeon, *Sens. Actuators, B*, 2018, **255**, 616–621.

210 J. Z. Ou, W. Ge, B. Carey, T. Daeneke, A. Rotbart, W. Shan, Y. Wang, Z. Fu, A. F. Chrimes, W. Wlodarski, S. P. Russo, Y. X. Li and K. Kalantar-zadeh, *ACS Nano*, 2015, **9**, 10313–10323.

211 K. Y. Ko, J.-G. Song, Y. Kim, T. Choi, S. Shin, C. W. Lee, K. Lee, J. Koo, H. Lee, J. Kim, T. Lee, J. Park and H. Kim, *ACS Nano*, 2016, **10**, 9287–9296.

212 H. Tabata, Y. Sato, K. Oi, O. Kubo and M. Katayama, *ACS Appl. Mater. Interfaces*, 2018, **10**, 38387–38393.

213 S. Zhao, G. Wang, J. Liao, S. Lv, Z. Zhu and Z. Li, *Appl. Surf. Sci.*, 2018, **456**, 808–816.

214 S. Shao, L. Che, Y. Chen, M. Lai, S. Huang and R. Koehn, *J. Alloys Compd.*, 2019, **774**, 1–10.

215 F. Perrozzi, S. M. Emamjomeh, V. Paolucci, G. Taglieri, L. Ottaviano and C. Cantalini, *Sens. Actuators, B*, 2017, **243**, 812–822.

216 Y. Han, Y. Liu, C. Su, S. Wang, H. Li, M. Zeng, N. Hu, Y. Su, Z. Zhou, H. Wei and Z. Yang, *Sens. Actuators, B*, 2019, **296**, 126666.

217 H. Tang, Y. Li, R. Sokolovskij, L. Sacco, H. Zheng, H. Ye, H. Yu, X. Fan, H. Tian, T.-L. Ren and G. Zhang, *ACS Appl. Mater. Interfaces*, 2019, **11**, 40850–40859.

218 K. C. Kwon, J. M. Suh, T. H. Lee, K. S. Choi, K. Hong, Y. G. Song, Y.-S. Shim, M. Shokouhimehr, C.-Y. Kang, S. Y. Kim and H. W. Jang, *ACS Sens.*, 2019, **4**, 678–686.

219 J. Wu, Z. Wu, H. Ding, Y. Wei, W. Huang, X. Yang, Z. Li, L. Qiu and X. Wang, *Sens. Actuators, B*, 2020, **305**, 127445.

220 X. Xin, Y. Zhang, X. Guan, J. Cao, W. Li, X. Long and X. Tan, *ACS Appl. Mater. Interfaces*, 2019, **11**, 9438–9447.

221 K. S. Kim, C. H. Ahn, S. H. Jung, S. W. Cho and H. Cho, *ACS Appl. Mater. Interfaces*, 2018, **10**, 10185–10193.

222 H.-S. Jeong, M.-J. Park, S.-H. Kwon, H.-J. Joo and H.-I. Kwon, *Sens. Actuators, B*, 2019, **288**, 625–633.

223 C.-S. Chu and M.-W. Hsieh, in *2017 25th Optical Fiber Sensors Conference (OFS)*, Jeju, 2017, pp. 1–4.

224 C.-S. Chu and M.-W. Hsieh, *Opt. Mater. Express*, 2019, **9**, 2937–2945.

225 C.-S. Chu and J.-C. Lo, in *Proc. SPIE 11205, Seventh International Conference on Optical and Photonic Engineering (icOPEN 2019)*, vol. 112050Y, 2019.

226 Y. H. Kim, K. Y. Kim, Y. R. Choi, Y.-S. Shim, J.-M. Jeon, J.-H. Lee, S. Y. Kim, S. Han and H. W. Jang, *J. Mater. Chem. A*, 2016, **4**, 6070–6076.

227 Y. Li, S. G. Leonardi, A. Bonavita, G. Neri and W. Wlodarski, *Procedia Eng.*, 2016, **168**, 1102–1105.

228 H. Karami and S. Babaei, *Int. J. Electrochem. Sci.*, 2013, **8**, 12078.

229 T. Fu, *Electrochim. Acta*, 2013, **112**, 230–235.

230 S. Yang, Y. Li, X. Wang, N. Huo, J.-B. Xia, S.-S. Li and J. Li, *Nanoscale*, 2014, **6**, 2582–2587.

231 M. Hafeez, U. Manzoor and A. S. Bhatti, *J. Mater. Sci.: Mater. Electron.*, 2011, **22**, 1772–1777.

232 H. Guo, C. Lan, Z. Zhou, P. Sun, D. Wei and C. Li, *Nanoscale*, 2017, **9**, 6246–6253.

233 J. Feng, L. Peng, C. Wu, X. Sun, S. Hu, C. Lin, J. Dai, J. Yang and Y. Xie, *Adv. Mater.*, 2012, **24**, 1969–1974.

234 A. Yang, J. Gao, B. Li, J. Tan, Y. Xiang, T. Gupta, L. Li, S. Suresh, J. C. Idrobo, T.-M. Lu, M. Rong and N. Koratkar, *2D Mater.*, 2016, **3**, 045012.

235 D. Burman, S. Santra, P. Pramanik and P. K. Guha, *Nanotechnology*, 2018, **29**, 115504.

236 Y. Luo, C. Chen, K. Xia, S. Peng, H. Guan, J. Tang, H. Lu, J. Yu, J. Zhang, Y. Xiao and Z. Chen, *Opt. Express*, 2016, **24**, 8956–8966.

237 B. Du, D. Yang, X. She, Y. Yuan, D. Mao, Y. Jiang and F. Lu, *Sens. Actuators, B*, 2017, **251**, 180–184.

238 Y. Feng, S. Gong, E. Du, K. Yu, J. Ren, Z. Wang and Z. Zhu, *J. Mater. Chem. C*, 2019, **7**, 9284–9292.

239 Y. Tan, K. Yu, T. Yang, Q. Zhang, W. Cong, H. Yin, Z. Zhang, Y. Chen and Z. Zhu, *J. Mater. Chem. C*, 2014, **2**, 5422–5430.

240 S. Yadav, P. Chaudhary, K. N. Uttam, A. Varma, M. Vashistha and B. C. Yadav, *Nanotechnology*, 2019, **30**, 295501.

241 L. Ze, G. Yueqiu, L. Xujun and Z. Yong, *Appl. Surf. Sci.*, 2017, **399**, 330–336.

242 N. Li, X. Chen, X. Chen, X. Ding and X. Zhao, *IEEE Electron Device Lett.*, 2017, **38**, 806–809.

243 D. Zhang, Y. e. Sun, P. Li and Y. Zhang, *ACS Appl. Mater. Interfaces*, 2016, **8**, 14142–14149.

244 Y. Zhang, H. Zou, J. Peng, Z. Duan, M. Ma, X. Xin, W. Li and X. Zheng, *Sens. Actuators, B*, 2018, **272**, 459–467.

245 G. U. Siddiqui, M. Sajid, J. Ali, S. W. Kim, Y. H. Doh and K. H. Choi, *Sens. Actuators, B*, 2018, **266**, 354–363.

246 D. Zhang, X. Zong and Z. Wu, *Sens. Actuators, B*, 2019, **287**, 398–407.

247 D. Zhang, X. Zong, Z. Wu and Y. Zhang, *Sens. Actuators, B*, 2018, **266**, 52–62.

This journal is © The Royal Society of Chemistry 2020

J. Mater. Chem. A, 2020, **8**, 24943–24976 | **24975**

248 D. Zhang, X. Zong, Z. Wu and Y. Zhang, *ACS Appl. Mater. Interfaces*, 2018, **10**, 32631–32639.

249 M. A. Dwiputra, F. Fadhila, C. Imawan and V. Fauzia, *Sens. Actuators, B*, 2020, **310**, 127810.

250 D. Zhang, Y. Cao, P. Li, J. Wu and X. Zong, *Sens. Actuators, B*, 2018, **265**, 529–538.

251 E. Espid and F. Taghipour, *Crit. Rev. Solid State Mater. Sci.*, 2017, **42**, 416–432.

252 M.-Y. Li, S.-K. Su, H. S. P. Wong and L.-J. Li, *Nature*, 2019, **567**(2), 169–170.

253 G. Q. Zhang, M. Graef and F. v. Roosmalen, in *56th Electronic Components and Technology Conference 2006*, IEEE, 2006, vol. 7.

254 G. Q. Zhang and A. van Roosmalen, *More than Moore: Creating High Value Micro/Nanoelectronics Systems*, Springer Science & Business Media, 2010.